Thin–Walled Structures 202 (2024) 112124

Contents lists available at ScienceDirect

Thin-Walled Structures

journal homepage: www.elsevier.com/locate/tws

Effects of steady-state fluid-structure interactions on air-supported membrane structures subjected to wind actions

Keye Yan [a,b,c], Yue Wu [a,b,c], Qiming Zhu [a,b,c,*], Zhaoqing Chen [d], Boo Cheong Khoo [e]

[a] *Key Lab of Structures Dynamic Behavior and Control of the Ministry of Education, Harbin Institute of Technology, Harbin 150090, China*
[b] *Key Lab of Smart Prevention and Mitigation of Civil Engineering Disasters of the Ministry of Industry and Information Technology, Harbin Institute of Technology, Harbin 150090, China*
[c] *School of Civil Engineering, Harbin Institute of Technology, Harbin 150090, China*
[d] *School of Civil Engineering and Architecture, Northeast Electric Power University, Jilin 132012, China*
[e] *Department of Mechanical Engineering, National University of Singapore, Singapore 117411, Singapore*

ARTICLE INFO

Keywords:
Air-supported membrane structure
Fluid-structure interaction
Time-averaged wind action
Simulation

ABSTRACT

With the perspective of static aeroelasticity, steady-state influences of fluid-structure interaction (FSI) on wind loads and responses of rectangular-planed air-supported membrane structure (ASMS) are investigated in this study. Steady-state FSI simulations are performed by coupling Reynolds-averaged computational fluid dynamics solving wind loads and static finite element analysis solving structural deformations. The feasibility of these simulations is validated with wind tunnel tests concerning time-averaged results. In contrast to analysis without static aeroelasticity, significant variations in wind pressure distributions and amplifications on structural wind responses due to steady-state FSI effects are observed. Subsequently, influencing factors and mechanisms of steady-state FSI effects are analyzed. These time-averaged effects are more significant with the increasing magnitude of structural wind actions, lower internal pressures and less membrane tensile stiffness. Though unlikely to induce irreversible effects as shell structures, the buckling of ASMS can make steady-state FSI more pronounced because of the coupling between stronger flow separation and larger membrane deformations. Accompanied with steady-state FSI, such buckling effect usually contributes to varying locations of the structural maximum responses and noticeable increases in response amplification factors, which deserves attentions in practice. Practically, it is realizable to evaluate these steady-state FSI effects above with simulations because of the much lower computational cost and reliable accuracy.

1. Introduction

As a special type of large-span structure, the air-supported membrane structure (ASMS) features itself by its unique way of spanning an enclosed space. The membrane, and usually reinforced with the cable net in engineering practice, is tensioned with the help of pressure differences. Such differences are usually maintained as several hundred pascals between indoors and outdoors by high-power air supply systems. ASMS originates from the early 20th century [1], and gradually gains its popularity because of its multiple advantages including less cost, rapid construction and lower carbon footprints. In recent years, ASMS has become an increasingly desirable option for large-span space structure constructions with a variety of purposes. For instance, public sports and exhibitions require a large-span enclosed space unaffected by harsh weathers, and some massive industrial facilities also need an enclosed zone to prevent air pollutions and other possible negative influences on environment. Hence, constructions of ASMS develop rapidly, and structural dimensions have successfully exceeded 100 m in recent engineering practices [2,3].

However, since the membrane acts as both load-bearing and cladding components, ASMS exhibits its noticeable sensitivity to extra loads, especially to wind actions. Wind-induced fluid-structure interaction (FSI) persists due to the lightweight and flexible nature within membrane. Usually referred as aeroelasticity, FSI is featured by the interactions among inertial forces, aerodynamic forces and elastic forces [4]. In detail, some phenomena involve all these three force components, such as buffeting, flutter and dynamic stability, and these are referred as dynamic aeroelasticity. On the contrary, other phenomena

---

* Corresponding author.
E-mail address: zhu_qiming@hit.edu.cn (Q. Zhu).

https://doi.org/10.1016/j.tws.2024.112124
Received 3 March 2024; Received in revised form 26 May 2024; Accepted 11 June 2024

only entail interactions between elastic forces and aerodynamic forces. These are defined as static aeroelasticity, including divergence and variations in load distribution. A schematic illustration of static and dynamic aeroelasticity is depicted in Fig. 1, with some of elements selected from the aeroelastic triangle of forces in the references [4,5].

Dynamic aeroelasticity has drawn major interests among a wide variety of research communities. For example, analytical approaches have been utilized to solve aerodynamic forces on airfoils, hence evaluating aerodynamic stability [4]. Analytical models are used to study the random vibration and coupling effect between different vibration modes of membrane structures [6,7]. Similar concepts have also been successfully applied by wind engineering, as the flutter derivatives obtained with forced-vibration experiments can be utilized to study aerodynamic stability of bridge decks [8]. The forced-vibration approach has also been adopted within aeroelastic studies concerning flow past bluff bodies, including circular cylinders [9–11] or square prisms [12–14]. Meanwhile, many aspects of FSI mechanisms related to dynamic aeroelasticity, such as vortex-induced vibrations, fluttering and galloping, have been explored on a variety of structures including large-span bridges [15,16], high-rise buildings [17–19] and cables [20,21]. Concerning membrane structures, a large number of researches concentrate on dynamic aeroelasticity [22–39]. These researches usually adopt the approach of analyzing the relations between structural modal motions and transient aerodynamic forces, which give rise to issues including aeroelastic instability and variations in structural modal parameters.

In contrast, however, attentions on static aeroelasticity seems much less intensive. As a member of static aeroelasticity, the FSI effect on time-averaged wind load distributions is usually evaluated less determinative to structural safety compared with the dynamic counterpart, at least for rigid-body research objects. Nevertheless, this steady-state FSI effect on the ASMS deserves attentions due to the following two concerns. One is the coupling between structural time-averaged deformations and wind pressures can be significant for the flexible membrane structures. For instance, Hincz et al. carried out wind tunnel tests to measure wind pressure distributions on two corresponding rigid models of a conical tensioned membrane structure [40]. Wind pressures are initially acquired with wind tunnel experiments on the first rigid model with the original geometry, and structural time-averaged wind-induced deformations are simulated with the obtained wind pressure distribution. Subsequently, the second rigid model with the deformed shape is subjected to the new wind pressure measurement test. Finally, remarkable differences of time-averaged wind load between the two rigid models have been observed. Besides, the FSI simulations on the saddle-shaped tensioned membrane structure performed by Sun and Gu have also discovered differences in mean wind pressure coefficients between the results with and without FSI, which is attributed to the altered surrounding flow distribution induced by structural deformations [41]. Moreover, the FSI simulations by De Nayer et al. on a hemispherical ASMS have also discovered variations in time-averaged fluid pressure coefficient with increasing inflow velocities, which is found related to the structural wind-induced deformations [42]. Two, the noticeable ratio of time-averaged part within structural total wind responses has also underscored the importance of investigating steady-state FSI effects. Some experimental and numerical studies on ASMS have observed that the magnitudes of root-mean-square (RMS) values of structural buffeting responses are usually only around 10 % of the time-averaged counterpart [42–44]. In other words, the steady-state component may constitute the majority of structural total wind responses for ASMS, thereby making the steady-state FSI effects non-neglectable when investigating the total wind-induced FSI influences. Nevertheless, different from the frequently studied dynamic aeroelasticity, steady-state FSI influences on wind actions on ASMS have not been systematically investigated as yet.

In contrast with featuring intricate mechanisms when studying dynamic aeroelasticity, the direct way to figure out the steady-state FSI effect is to compare results of time-averaged wind loads and structural wind responses with and without FSI. Numerical simulations thus become a viable approach, as structural responses "without FSI" cannot be directly observed during aeroelastic experiments. With the development of algorithms and computational capabilities, methods simulating FSI effects of membrane structures have become feasible and efficient. Glück et al. proposed the coupling scheme to simulate FSI effects by combing the computational fluid dynamic (CFD) module in the fluid region and the finite element method (FEM) module for structural analysis, and information between these two modules are communicated with the coupling algorithm [45]. This coupling scheme has been further developed to enable detailed analysis on tensioned membrane structures subjected to wind actions [46–48]. Based on FSI simulations coupling isogeoemtric FEM analysis and large eddy simulation CFD with variational multiscale method, Zhu et al. carried out aeroelastic studies on low-roof structures [49]. Yang et al. performed fully-coupled FSI simulations on an enclosed planar tensioned membrane subjected to wind actions to study the mechanisms of energy transfer and aerodynamic instability [50]. As for studies on ASMS, De Nayer et al. [42] implemented transient FSI simulations on a hemispherical model to analyze and complement the experimental findings of aeroelastic wind tunnel tests by Wood et al. [51], subsequently with simulations on effects of gust winds on such structure [52,53].

These simulation methods introduced above are developed with motivations of simulating transient FSI effects. However, despite increasingly accurate solutions, implementing transient simulations on membrane structures with FSI effects require extremely high computational effort. Still, compared with transient FSI analysis, performing steady-state FSI simulations is far less demanding and efficient if one only requires to investigate the time-averaged properties. For instance, Lund et al. proposed the application of the steady-state FSI simulation in

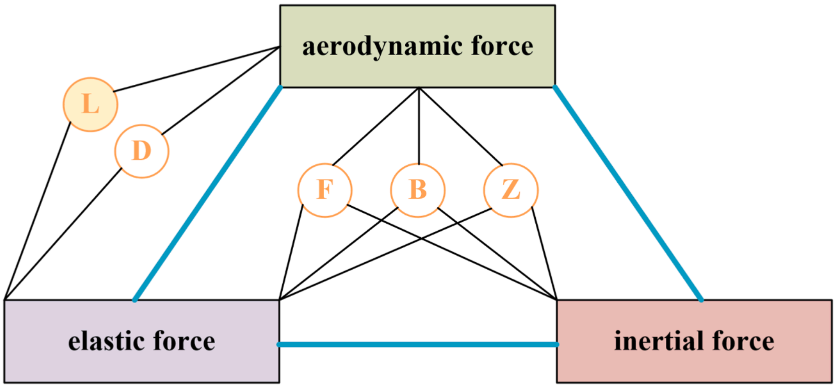

Fig. 1. Some selected elements in the aeroelastic triangle of forces [4,5]. F: flutter; B: buffeting; Z: dynamic response; L: load distribution; D: divergence. The time-averaged component within part "L" (load distribution) is the research motivation of this study.

structural shape optimizations [54]. Yoon has developed topology optimization using a monolithic procedure with the stationary FSI scheme [55]. Maljaars et al. adopted the steady-state approach to develop FSI simulation methods for periodic problems [56]. López et al. investigated an elasto-flexible membrane blade in a non-rotating configuration with steady-state FSI simulations, and analyzing the differences of aerodynamic characteristics between the flexible blade and the rigid counterpart [57]. Using the steady-state FSI scheme, Silva et al. carried out topology optimization of binary structures with geometry trimming [58].

Motivated by the importance of static aeroelasticity and the feasibility of time-averaged FSI simulation for ASMS, this work aims to implement steady-state FSI simulations on ASMS subjected to wind actions by coupling stationary CFD and static structural FEM analysis. Simulations are firstly validated by time-averaged results of wind tunnel tests on rigid and aeroelastic experiments. In addition, as multiple stationary FSI simulations are realizable with respect to computational costs, a variety of simulations are carried out to study influencing factors and mechanisms of steady-state FSI.

2. Simulation methods

2.1. Structural geometry

Rectangular-planed ASMS with length L, width B and height H are analyzed in this study as shown in Fig. 2. Different from the planar or saddle-shaped geometries, which have been frequently adopted in studies on tensioned membrane structures, shapes of rectangular-planed ASMS in this study cannot be expressed with simple analytical forms. Instead, structural geometries are obtained with the form-finding approach using FEM [59,60]. The form-finding procedures can be summarized as follows: (1) meshing the rectangular planar surface with the size of $L \times B$; (2) transforming the planar surface into curved geometry by applying upward pressures; (3) achieving the target height H by adjusting parameters including material properties and pressures to finalize the structural shape configuration.

2.2. Setup of the CFD simulation

Configurations of the CFD simulation are presented here, which is a key component within steady-state FSI simulations. The computational domain and mesh are shown in Fig. 3. The blocking ratios are less than 5 % in the all numerical setup. Structured cells are generated in the computation domain using the software ICEM CFD 2020 R2. Three different types of mesh configurations are tested, and mesh sensitivity analysis results are presented in Table 1. Within the basic grids, the nondimensional wall distance $y+$ of the first layer mesh on the membrane surface is achieved around 1.0 to resolve turbulence fine scale at the near wall location. The coarse grids are generated by coarsen the basic mesh in all three dimensions. Simulation results with the coarse grid exhibit noticeable differences compared with the other two mesh configurations, and as presented in Section 3.1, results with the coarse grid also have obvious deviations from experimental observations. On the contrary, the fine grids are developed with refinements at the membrane surface of the basic grids along the x and y directions. Results of wind loads on the membrane surface suggest that simulation results generally remain unchanged after refining mesh based on the basic grid. Therefore, the basic grid configuration is adopted in this research because of its feasibility and efficiency.

Since the present work focuses on time-averaged wind effects only, the approach employing the Reynolds-averaged Navier-Stokes (RANS) equations is adopted to simulate time-averaged properties of the incompressible air flow with turbulence [61]:

$$\frac{\partial \overline{u}_i}{\partial x_i} = 0 \tag{1}$$

$$\frac{\partial \overline{u}_i}{\partial t} + \frac{\partial \overline{u}_j \overline{u}_i}{\partial x_j} = -\frac{1}{\rho}\frac{\partial \overline{p}}{\partial x_i} + \frac{\partial}{\partial x_j}\left(\upsilon \frac{\partial \overline{u}_i}{\partial x_j} - \overline{u'_I u'_J}\right) \tag{2}$$

where $\overline{u}_i$ and u'_i are time-averaged and fluctuating components of wind velocities respectively, $\overline{p}$ is the mean pressure, and the term $-\overline{u'_I u'_J}$ usually referred to as the Reynolds stress is solved by turbulence models. In this study, the renormalization group theory (RNG) k-ε model is applied for the RANS computations [61]. That is,

$$\overline{u'_i u'_j} = \frac{2}{3} k \delta_{ij} - \upsilon_t \left(\frac{\partial \overline{u}_i}{\partial x_j} + \frac{\partial \overline{u}_j}{\partial x_i}\right) \tag{3}$$

$$\frac{\partial k}{\partial t} + \frac{\partial \overline{u}_j k}{\partial x_j} = D_k + P_k - \varepsilon \tag{4}$$

$$\frac{\partial \varepsilon}{\partial t} + \frac{\partial \overline{u}_j \varepsilon}{\partial x_j} = D_\varepsilon + P_\varepsilon - C_{\varepsilon 2}\frac{\varepsilon^2}{k} \tag{5}$$

$$\begin{aligned} \upsilon_t = C_\mu \frac{k^2}{\varepsilon},\ D_k = \frac{\partial}{\partial x_j}\left(\frac{\upsilon_t}{\sigma_k}\frac{\partial k}{\partial x_j}\right),\ P_k = \frac{1}{2}\upsilon_t\left(\frac{\partial \overline{u}_i}{\partial x_j} + \frac{\partial \overline{u}_j}{\partial x_i}\right)^2,\ D_\varepsilon \\ = \frac{\partial}{\partial x_j}\left(\frac{\upsilon_t}{\sigma_\varepsilon}\frac{\partial \varepsilon}{\partial x_j}\right),\ P_\varepsilon = C_{\varepsilon 1}\frac{\varepsilon}{k}P_k \end{aligned} \tag{6}$$

where δ_{ij} is the Kronecker delta function, k is turbulent kinetic energy, ε is turbulent dissipation rate, υ_t is turbulent eddy viscosity, D_k and D_ε are dissipation terms for k and ε respectively, and P_k and P_ε are production terms for k and ε respectively. Typical coefficients are: $C_\mu = 0.0845$, $\sigma_k = 0.72$, $\sigma_\varepsilon = 0.72$, $C_{\varepsilon 1} = 1.42$, $C_{\varepsilon 2} = 1.68$.

CFD simulations are performed with the software ANSYS Fluent 2020 R2 using the finite volume method (FVM), and the SIMPLE scheme is used for discretion of all transport equations with a second-order scheme. To model the atmospheric boundary layer, wind velocity and turbulence intensity profiles of the inlet boundary are adopted as follows with the type B terrain roughness in Chinese load code, which refers to

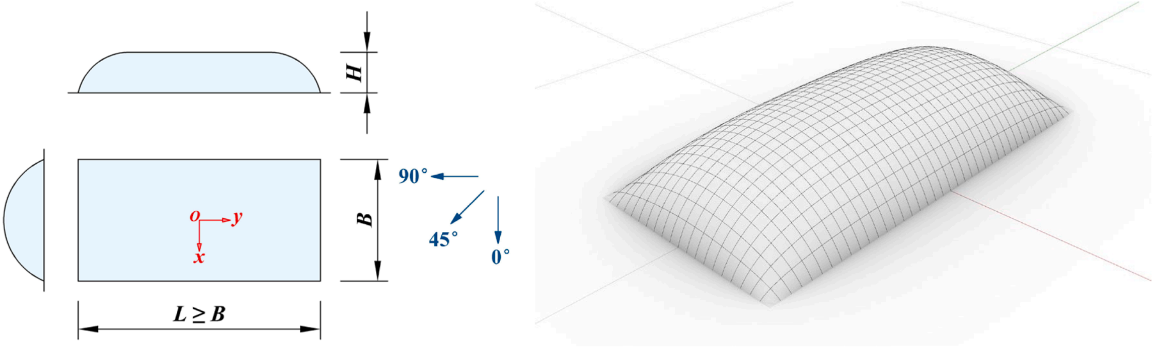

Fig. 2. Geometry of the rectangular-planed ASMS.

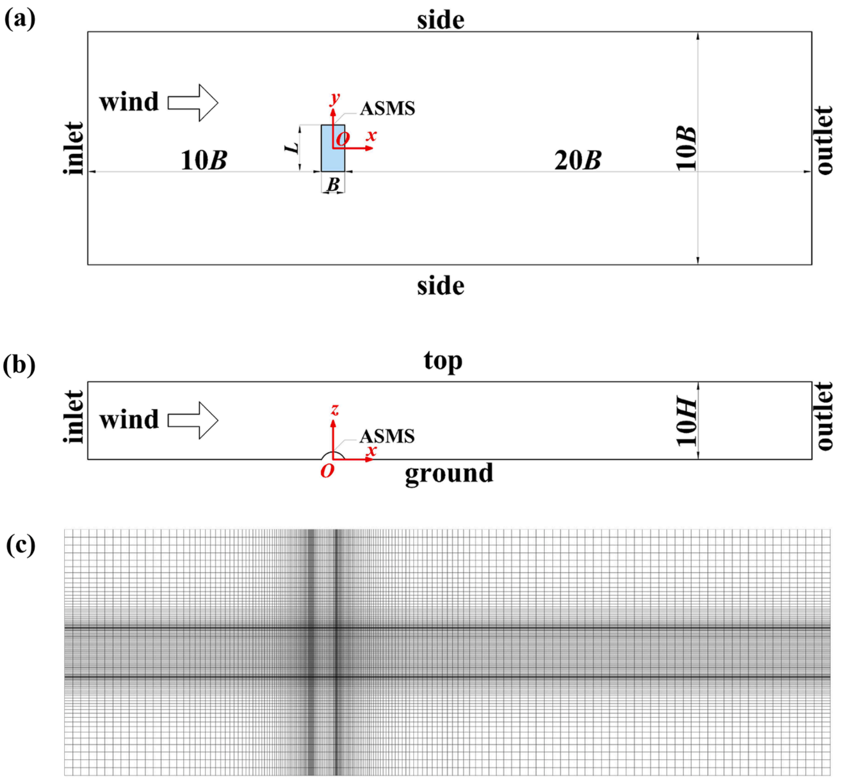

Fig. 3. CFD computational setup ($L\times B\times H$= 1.2 m × 0.6 m × 0.2 m, 0° wind direction). (a) Top view of the computational domain; (b) Side view of the computational domain; (c) Top view of the mesh (basic grid).

Table 1
Mesh sensitivity analysis ($L\times B\times H = 1.2\,m\times 0.6\,m\times 0.2$ m, 0° wind direction).

Mesh layout	Coarse grid	Basic grid	Fine grid
Total cell number (million)	0.85	1.92	4.31
Grid layouts on the membrane surface	20 × 40	30 × 60	40 × 80
Wind force coefficient along x-axis C_{Fx}	0.20	0.17	0.17
Wind force coefficient along z-axis C_{Fz}	0.44	0.49	0.49
Maximum wind pressure coefficient $C_{p,\max}$	0.60	0.64	0.64
Minimum wind pressure coefficient $C_{p,\min}$	−1.19	−1.27	−1.28

fields and towns with sparse housing [62].

$$U(z) = \begin{cases} U_{10}\left(\dfrac{z}{z_b}\right)^{\alpha} & z_b \le z \le z_g \\ U_{10} & z < z_b \end{cases} \tag{7}$$

$$I_u(z) = \begin{cases} I_{u,10}\left(\dfrac{z}{z_{10}}\right)^{-\alpha} & z_b \le z \le z_g \\ I_{u,10} & z < z_b \end{cases} \tag{8}$$

Parameters for these formulas are given in Table 2.

Table 2
Constants of Eq. (7) and (8) for the scaled model and the prototype.

Symbol	Meaning	Value (scaled model)	Value (prototype)
α	Roughness index	0.15	0.15
z_g	Gradient height (m)	3.5	350
z_b	Truncation height (m)	0.1	10
z_{10}	Reference height for turbulence intensity (m)	0.1	10
U_{10}	Wind velocity at z_b (m/s)	10	30
$I_{u,10}$	Turbulence intensity at z_b	0.14	0.14

To satisfy profiles in Eqs. (7) and (8), turbulent kinetic energy k and turbulent dissipation rate ε of the inlet boundary are set as [63]

$$k(z) = 1.5\left(I_u(z)U(z)\right)^2 \tag{9}$$

$$\varepsilon(z) = \frac{k(z)^{\frac{3}{2}}}{l} \tag{10}$$

Here, l is the turbulence length scale. Pressure outlet condition are adopted at the outlet boundary. No-slip wall conditions and enhanced wall treatment are set for the membrane surface and ground, and symmetrical boundary conditions are applied for the side and top boundaries of the computational domain.

To evaluate wind pressure distributions on the structure, the dimensionless wind pressure coefficient is determined as:

$$C_p = \frac{P - P_0}{0.5\rho U_r^2} \tag{11}$$

where P is wind pressure, P_0 and U_r are pressure and wind velocity at reference height z_r respectively, and ρ is density of the air. The reference height z_r is adopted as 0.2 m. Meanwhile, dimensionless wind force coefficients are acquired as:

$$\begin{cases} C_{Fx} = \dfrac{\sum_{i=1}^{N_p} F_i\cdot\hat{i}}{0.5\rho U_r^2 LH} \\ C_{Fy} = \dfrac{\sum_{i=1}^{N_p} F_i\cdot\hat{j}}{0.5\rho U_r^2 BH} \\ C_{Fz} = \dfrac{\sum_{i=1}^{N_p} F_i\cdot\hat{k}}{0.5\rho U_r^2 LB} \end{cases} \tag{12}$$

where C_{Fx}, C_{Fy}, C_{Fz} are the wind force coefficients in the x, y, z directions respectively; F_i is the nodal wind force vector of tap i, which is derived from the pressure coefficient and the tributary area; and $\hat{i}$, $\hat{j}$, $\hat{k}$ are the unit vectors in x, y, z directions.

As this study focuses on steady-state wind actions only, C_p, C_{Fx}, C_{Fy} and C_{Fz} refer to time-averaged values when processing data from wind tunnel tests during experimental validations. Moreover, the reference wind velocity U_r is applied to describe variations in wind speeds in subsequent discussions.

2.3. *Setup of the structural analysis*

The FEM module for structural analysis is achieved by the Mechanical application within ANSYS Workbench 2020 R2. After importing the geometry, the structure is discretized into triangular membrane elements, and the edge of each element is with the size around $B/25$. The fixed support boundary condition is applied on the edges of the curved membrane, and the internal pressure P_{in} is applied as the surface pressure on the membrane. The term "internal pressure" in this study means the pressure difference between the internal volume of the ASMS and the atmosphere. The Newton-Raphson method is applied to solve the numerical problem, and the geometric nonlinearity is considered within numerical iterations.

2.4. *Setup of the steady-state FSI simulation*

The software ANSYS Workbench 2020 R2 is used for simulating time-averaged FSI effects on ASMS, where information of the Mechanical module for structural analysis and the Fluent module for CFD is communicated by the System Coupling module. Within the Fluent module, the dynamic mesh in CFD simulation is required to achieve accordance between membrane movement from the FEM analysis and the moving boundary in the CFD computational domain. In the simulation, the computation mesh is updated by the diffusion-based smoothing method, where the mesh motion is governed by the diffusion equation [63]. Meanwhile, the dynamic mesh type of the membrane surface is set as System Coupling, and other settings of CFD simulations are the same as discussed in Section 2.2. Correspondingly, within the Mechanical module, the Fluid Solid Interface is set on the membrane to enable interactions with System Coupling. A brief summary on FSI simulation settings is presented in Table 3.

To illustrate the feasibility and importance of steady-state FSI simulations, two computational strategies are performed and compared here. One strategy is the 2-way coupling simulation described above, which is mainly applied in this study. Another strategy is referred as the 1-way simulation, in which wind pressures on the rigid model acquired by CFD are directly applied on FEM models of the membrane, without feedbacks of structural deformations on wind loads. The 1-way method is a common practice in the structural design of buildings, but as discussed in the following sections, the 1-way strategy becomes inapplicable when dealing with flexible structures subjected to noticeable stationary FSI effects, while the 2-way coupling strategy is still feasible.

Table 3
Computational settings of steady-state FSI simulation.

Simulation part	Configuration
Fluid	Solver: ANSYS Fluent 2020 R2 Spatial discretion: Second-order for all transport equations Solving method: SIMPLE Boundary Condition (BC) for inlet: Velocity inlet BC for outlet: Pressure outlet BC for membrane surface and ground: non-slip wall BC for side and top: Symmetry
Membrane	Solver: Mechanical module in ANSYS Workbench 2020 R2 Solving method: Newton-Raphson with geometric nonlinearity BC: Fixed at membrane edges
Coupling	Communication between fluid and membrane: System Coupling module in ANSYS Workbench 2020 R2 CFD mesh adaption: Diffusion-based smoothing method in ANSYS Fluent 2020 R2

To determine the proper number of iteration steps between the FEM and CFD modules, simulation results of wind loads and structural responses with different iteration numbers are presented in Fig. 4. Five FSI iteration steps are finally adopted, as results remain unchanged with further iterations. The computation is performed on the PC machine with AMD Ryzen 7 3700 × 8-cores CPU and 32 GB memory, and each case takes approximately 9.3 CPU hours, featuring its much less computation costs compared with transient simulations, whose time costs are usually at the level of 10^4 CPU hours [42,50]. Therefore, with the perspective of computational efficiency, the steady-state simulation is a viable option if one only requires to study the time-averaged part of FSI instead of the full transient results.

Variations of the following parameters are included in the simulations and experimental validations: wind directions, structural geometry parameters $L \times B \times H$, wind velocities U_r, internal pressures P_{in} and membrane tensile stiffness $E_m h$ (E_m is membrane elastic modulus and h is membrane thickness). The poisson ratio of the membrane is set as 0.3.

2.5. *Similarity analysis*

With the convenience in performing experimental validations, all steady-state FSI simulations in this study are carried out on scaled ASMS models. Therefore, the similarity analysis is required to evaluate the correspondence between models and prototypes. Several similarity parameters are given with respect to tensioned membrane subjected to wind actions [23,64]. Since this study only concentrates on time-averaged properties, the following similarity rules are proposed:

1. Two basic similarity parameters are determined firstly: the length scale λ_B and the wind velocity scale λ_U with respect to the width B and the reference wind speed U_r.
2. The internal pressure scale λ_P: To describe the ratio between internal pressure P_{in} and wind load, the dimensionless number $P_{in}/\left(\rho U_r^2\right)$ is proposed, which should be the same for the prototype and scaled model. Hence, the internal pressure scaling ratio is derived as $\lambda_P = \lambda_U^2$.
3. The membrane tensile stiffness scale λ_{Eh} is linked with the dimensionless number $E_m h/\left(\rho U_r^2 B\right)$, which describes combined effects of wind pressure and membrane elasticity. As such, the value λ_{Eh} is equal to $\lambda_U^2 \lambda_B$. Moreover, the membrane thickness ratio $\lambda_h = \lambda_B$ and the elastic modulus ratio $\lambda_E = \lambda_U^2$ can also be derived based on the dimensional harmony principle.

Specific values of these scaling parameters above are presented in subsequent discussions. Within aeroelastic wind tunnel tests, not all similarity requirements can be fulfilled due to experimental availability and selected research objective. However, for all steady-state FSI simulations, these scaling requirements can be all achieved by adopting proper parameters.

3. Experimental validations

3.1. *Validating the CFD simulation: time-averaged wind loads on rigid models*

CFD simulations are verified with wind pressure distributions acquired by wind tunnel tests on the corresponding rigid model. Experiments are performed in the Joint Laboratory of Wind Tunnel and Wave Flume at Harbin Institute of Technology, and this closed-circuit boundary layer wind tunnel is with length of 25 m, width of 4 m and height of 3 m. The rigid model is with the size of $L \times B \times H$=1.2 m × 0.6 m × 0.2 m, and wind profiles are as presented in Section 2.2. Wind pressures on the model with the 0° wind direction are investigated here, and pressure measurement taps are installed on the surface of the rigid model, which are connected to pressure scanning valves with sampling

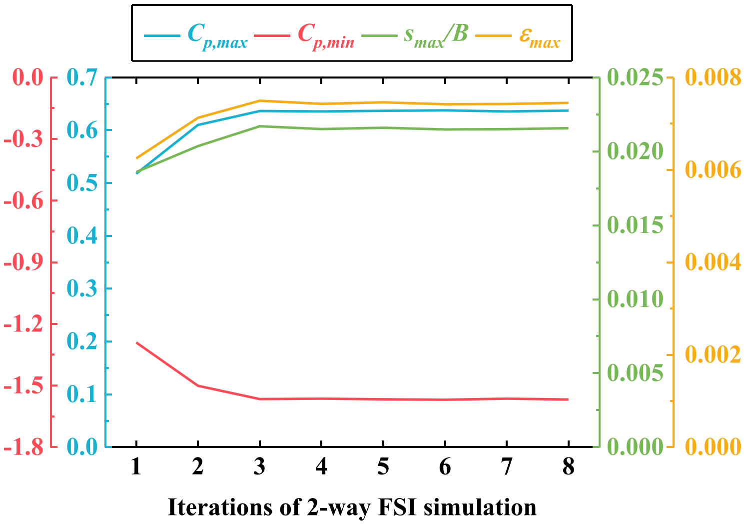

Fig. 4. Variations of wind load and structural response results with different iteration times of 2-way FSI coupling simulation. ($L \times B \times H$= 1.2 m × 0.6 m × 0.2 m, P_{in} = 100 Pa, U_r = 12 m/s, $E_m h$ = 4000 N/m).

frequency of 625 Hz and sampling duration of 20 s. The standard error of the mean, defined as the standard deviation divided by the square root of the sample size, is calculated to evaluate uncertainties within measured time-averaged values.

Fig. 5 presents comparisons of CFD simulation results and time-averaged wind pressures obtained from wind tunnel tests, and results with all the three mesh configurations in Table 1 are presented to supplement the mesh sensitivity analysis. Standard errors of time-averaged wind pressure coefficients on all measurement points are less than 5×10^{-3}. Wind pressure distributions of both the basic and the fine mesh are close to the experimental results, while simulations with the coarse mesh are with obvious deviations, hence making available the basic configuration in subsequent simulations. In addition, results in Fig. 4 also exhibits characteristics of wind pressure distributions. Wind pressure forces are observed on the windward surface, and top locations of the model exhibit effects of obvious wind suction forces. Meanwhile, slight wind suction forces are also discovered on the leeward surface. As discussed later, these characteristics can directly affect patterns of structural wind responses.

3.2. *Validating the steady-state FSI simulation: aeroelastic wind tunnel tests*

The steady-state FSI simulations are verified with results of aeroelastic wind tunnel tests, with experimental methods similar to studies on spherical or capsule-shaped ASMS [65,66]. With the geometry of $L \times B \times H$=1.2 m × 0.6 m × 0.2 m, the rectangular-planed ASMS aeroelastic model is made of PVC membrane with thickness h = 0.14 mm and elastic modulus E_m = 16 MPa. Similarity analysis on the aeroelastic wind tunnel

Table 4
Similarity parameters of the aeroelastic wind tunnel test.

Property	Theoretical scaling ratio	Values (scaled model)	Values (prototype)	Actual scaling ratio
Span B	1:100	0.6 m	60 m	1:100
Wind velocity U_r	1:2	11 m/s	22 m/s	1:2
Internal Pressure P_{in}	1:4	100 Pa	400 Pa	1:4
Membrane tensile stiffness $E_m h$	1:400	2240 N/m	10^6 N/m	1:446

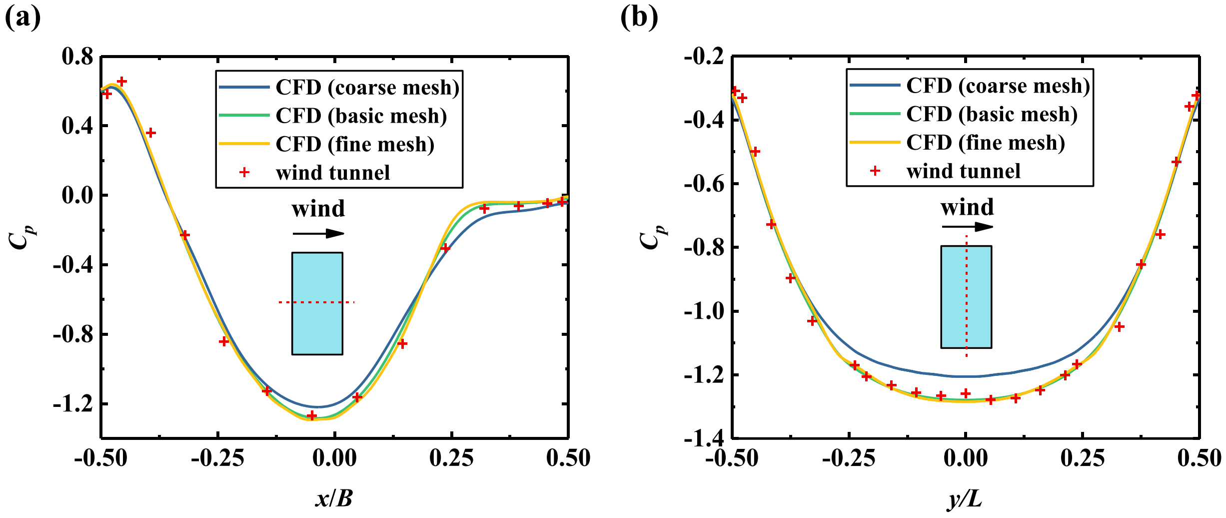

Fig. 5. Comparison of C_p values between wind tunnel tests and CFD simulations. (a) C_p along the x axis; (b) C_p along the y axis.

test is provided in Table 4. The elastic modulus and thickness of the prototype are adopted as 1000 MPa and 1 mm respectively, which are realizable in practice [67]. Wind profiles of aeroelastic tests are the same as given in Eq. (7) and (8), with wind velocity U_r equals to 11 m/s.

Wind induced displacements of the membrane surface are acquired by stereo digital image correlation (3D-DIC), which has also been applied in previous aeroelastic studies on ASMS [51]. Theoretical backgrounds of 3D-DIC have been illustrated within the reference [68]. The 3D-DIC system (Stereo-3D, MatchID) includes two cameras (Computar M2518-MPW2), an image acquisition system and the image processing software. To measure structural deformations, speckle patterns are drawn on aeroelastic models as in Fig. 6. Two cameras are placed at different angles to achieve 3D reconstruction of structural geometries from two planar pictures, and photos on a calibration plate have been utilized to acquire intrinsic and extrinsic parameters of the two cameras. During wind tunnel experiments, cameras are placed outside the wind tunnel to avoid influences of wind fluctuations on measurements. Thus, to acquire the deformation of all the membrane surface, measurements have been performed with two different configurations of camera locations, and results of different locations are integrated during post-processing to obtain the full-field time-averaged deformation results. A single image sampling process is with the duration of 10 s and the frequency of 30 Hz. Each measure produces 300 pairs of photographs with resolution of 2592×2048. The total deformation of a single point on membrane surface is $s = \sqrt{u^2 + v^2 + w^2}$, where u, v, w are deformations in the three orthogonal directions, and the time-averaged value of experimental results is adopted for the validations.

Fig. 7 gives the comparisons of time-averaged structural deformations among the aeroelastic wind tunnel test, the 1-way simulation and the 2-way coupling FSI simulation. Standard errors for all time-averaged values of measured s/B in experiments are within 1.3×10^{-4}. Due to wind load characteristics, distribution patterns of structural wind responses are similar in all three cases. The largest wind responses are found on top locations due to wind suction, and obvious windward deformations induced by wind pressure forces. Despite some slight deviations, results of the 2-way coupling steady-state FSI simulation are close to the wind tunnel experiments, hence proving the feasibility of such simulation method. In contrast, noticeable difference persists between 2-way coupling and 1-way simulation results, highlighting the influences of time-averaged structural deformations on steady-state wind loads of the ASMS with the FSI scheme.

4. Discussions on factors influencing steady-state FSI

After validating the feasibility of the steady-state FSI simulation method for analyzing wind actions on ASMS, influences of multiple factors on time-averaged FSI effects are investigated next, encompassing variations in wind direction, structural geometry, wind pressure, internal pressure and membrane tensile stiffness.

4.1. Effects of wind directions

For simplicity, wind and structural parameters are set as the values given in Table 5 when discussing influences of varying wind directions on the steady-state FSI effect. Meanwhile, definitions of wind directions are shown as in Fig. 2.

Table 6 presents variations in some of wind load parameters with different wind angles. Simulation results of both with and without FSI suggest that effects of wind action get milder as the azimuth varies from 0° to 90° Obvious influences of FSI on the minimum C_p values are observed, while FSI-induced differences with respect to wind force coefficients C_{Fx}, C_{Fy}, C_{Fz} and the maximum C_p values are relatively moderate. In this way, it can be presumed that the steady-state FSI effect may contribute to variations in wind pressure distribution patterns.

Fig. 8 gives examples of the C_p distributions at wind angles of 0°, 45° and 90°, respectively. Differences between the 2-way coupling FSI simulation and the CFD-only calculation are most noticeable with 0° wind angle, where the wind suction zone becomes more concentrated and intensive with increasing wind suction forces influences by FSI effects. Despite relatively less magnitudes, the steady-state FSI effects also deserve attentions for the other wind directions, as the 2-way coupling simulations can still lead to differences from the results without FSI.

With the FSI scheme, variations in wind pressure distributions are usually accompanied with changes in structural wind-induced displacements. As magnitudes of wind loads and structural stiffness to resist wind actions along the 0° direction are noticeably lower than those along the 90° direction for the geometry investigated here, structural deformations gradually get reduced as the wind angle shifts from 0° to 90° as depicted in Fig. 9. Moreover, since larger deformations usually result in more noticeable FSI influences, Fig. 9 also reveals variations in differences of structural deformations induced by FSI effects with wind directions, and locations of structural maximum displacements generally correspond to zones where wind pressures vary significantly as depicted in Fig. 8.

Membrane strain is also an important aspect of structural responses, as it is directly linked to structural safety. Supposing the membrane with linear elasticity, the strain distribution can also provide structural stress information. Fig. 10 gives results of structural total strain with and without FSI effects, and FSI-induced strain variations are clearly observed at 0° to 45° on the top locations. Structural strain varies only slightly with the 90° wind direction, possibly because structural total stress primarily constitutes of prestress with internal pressures, while

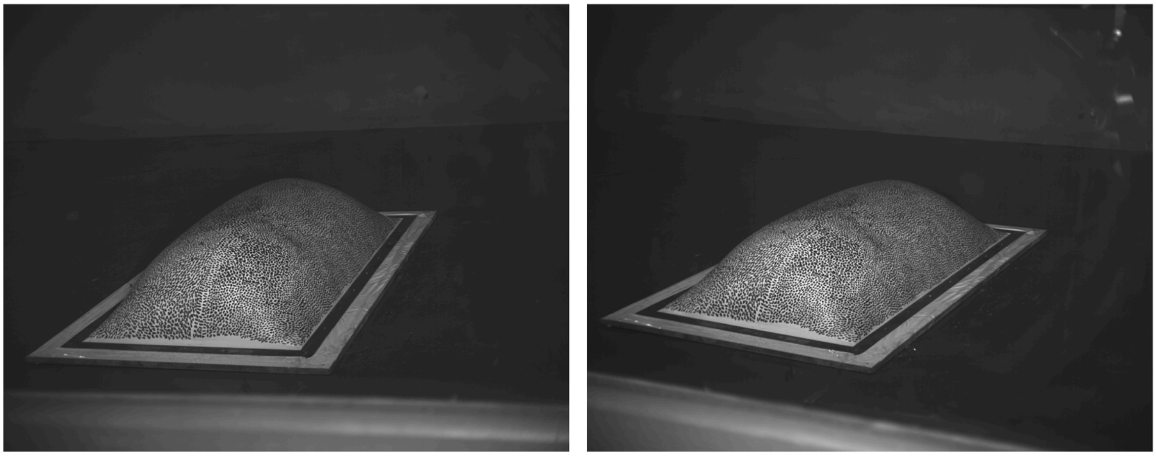

Fig. 6. Photos of speckled ASMS models from two cameras during aeroelastic experiments.

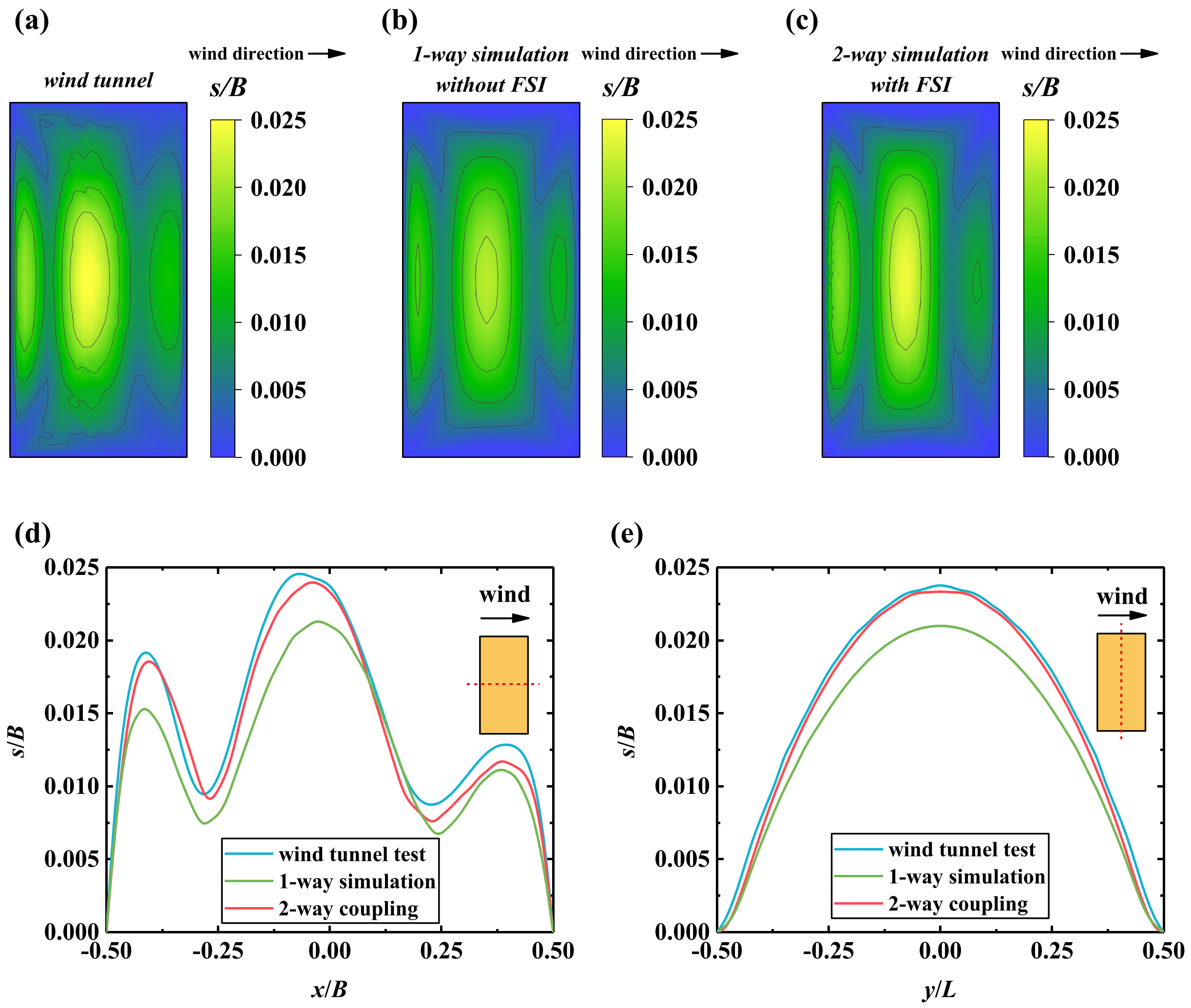

Fig. 7. Comparisons of structural wind induced displacements obtained from the aeroelastic wind tunnel test, the 1-way simulation and the 2-way coupling FSI simulation. (a) s/B (wind tunnel tests); (b) s/B (1-way simulation); (c) s/B (2-way coupling FSI); (d) s/B along the x axis; (e) s/B along the y axis.

Table 5
Parameters in discussions with varying wind directions.

Parameter	Value
Geometry $L \times B \times H$ (m)	$1.2 \times 0.6 \times 0.2$
Wind velocity U_r (m/s)	12
Internal pressure P_{in} (Pa)	100
Membrane tensile stiffness $E_m h$ (N/m)	4000
Membrane thickness h (m)	10^{-5}
Membrane elastic modulus E_m (MPa)	400

effects of the wind-induced stress are insignificant with this wind angle.

To evaluate steady-state FSI effects on structural responses, the amplification factors for structural maximum wind-induced displacements and maximum principal strain, β_s and β_ε are proposed as:

$$\beta_s = \frac{s_{max,\ FSI}}{s_{max,ref}} \tag{13}$$

$$\beta_\varepsilon = \frac{\varepsilon_{max,\ FSI}}{\varepsilon_{max,ref}} \tag{14}$$

where $s_{max,\ FSI}$ and $s_{max,ref}$ are structural maximum wind-induced displacement values with 2-way coupling and 1-way simulations respectively, and $\varepsilon_{max,\ FSI}$ and $\varepsilon_{max,ref}$ are membrane maximum principal

Table 6
Steady-state FSI effects on wind load characteristics with varying wind directions.

Wind direction	C_{Fx}		C_{Fy}		C_{Fz}		Maximum C_p		Minimum C_p	
	FSI	CFD	FSI	CFD	FSI	CFD	FSI	CFD	FSI	CFD
0°	0.21	0.17	0.00	0.00	0.49	0.49	0.64	0.64	−1.59	−1.29
15°	0.21	0.17	0.19	0.15	0.48	0.49	0.63	0.62	−1.57	−1.28
30°	0.18	0.15	0.29	0.23	0.47	0.46	0.61	0.61	−1.50	−1.21
45°	0.13	0.11	0.24	0.19	0.40	0.39	0.57	0.56	−1.47	−1.28
60°	0.11	0.10	0.18	0.16	0.30	0.30	0.60	0.59	−1.30	−1.14
75°	0.08	0.07	0.10	0.14	0.24	0.23	0.65	0.63	−0.93	−0.82
90°	0.06	0.06	0.00	0.00	0.21	0.20	0.66	0.64	−0.46	−0.40

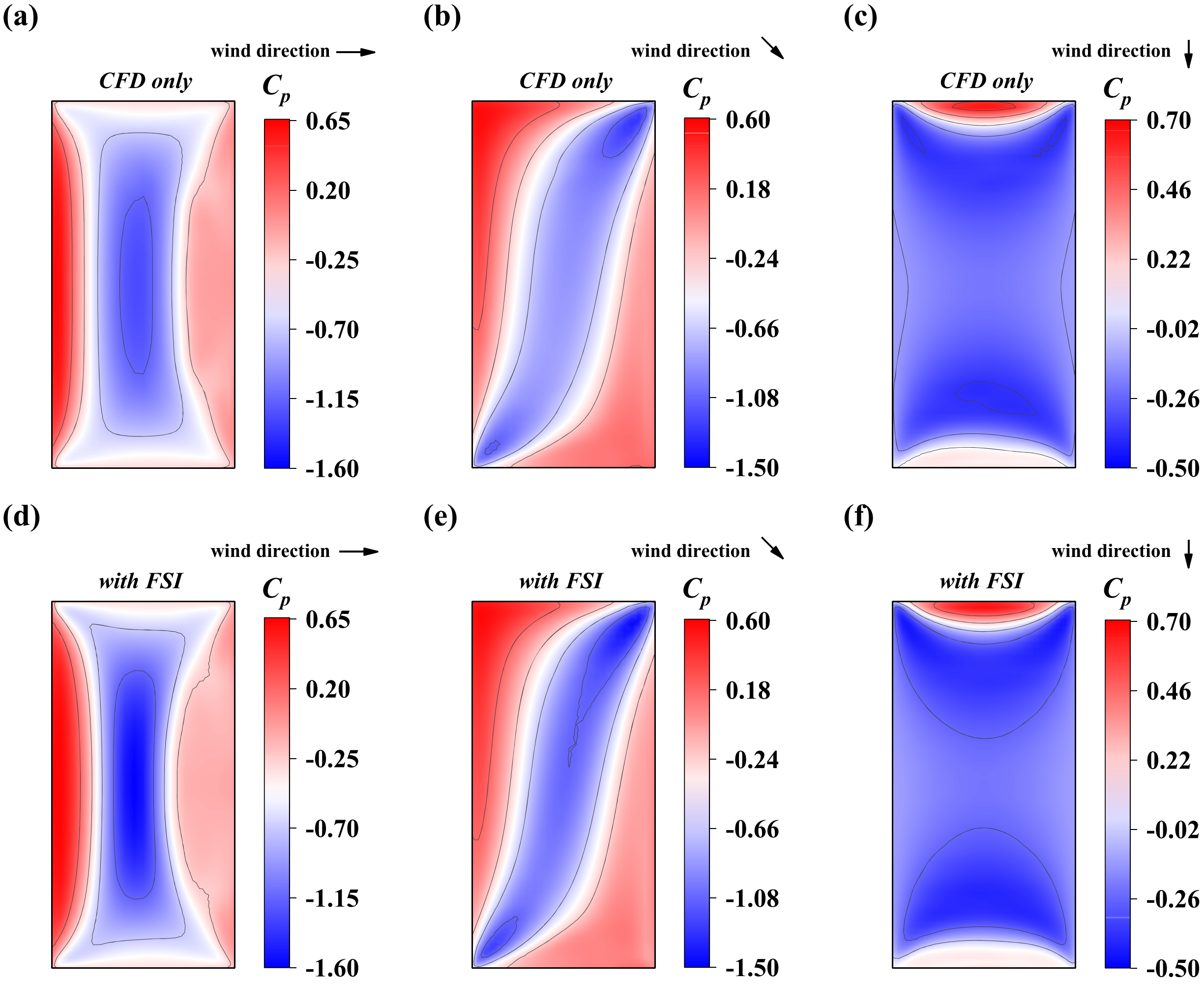

Fig. 8. Steady-state FSI effects on wind pressure distributions with different wind directions. (a) 0°, CFD only; (b) 45°, CFD only; (c) 90°, CFD only; (d) 0°, 2-way coupling FSI; (e) 45°, 2-way coupling FSI; (f) 90°, 2-way coupling FSI.

strain values with 2-way coupling and 1-way simulations respectively. Obviously, these two factors should be identical if structures exhibit linear responses to extra loads. However, β_s and β_ε are usually different when investigating ASMS as in this study because of noticeable geometric nonlinearity within membrane structures. Table 7 shows values of β_s and β_ε with different wind angles. The strain amplification factor β_ε is maximum with the 0° wind direction, at which the steady-state FSI effect can increase the maximum principal strain by about 8 %. Variations of β_s values with wind directions are rather complex, but significant FSI-induced quantity rises in wind-induced displacements are observed at all wind angles with the increase of up to 21 %. Moreover, β_s values are usually larger than β_ε, suggesting strain redistributions within ASMS due to large deformations, thereby result in reduced strain increments and more pronounced displacements induced by the steady-state FSI effect.

These results above indicate the importance of accounting the steady-state FSI effect with all wind angles, especially when wind direction aligns with the direction at which the structure has the lowest stiffness. In the following sections, only cases with 0° direction are investigated because of its most noticeable FSI effects.

4.2. Effects of structural geometry

When discussing influences of structural geometry, parameters are kept same as Table 5 except the $L \times B \times H$ configuration. Table 8 lists all analyzed geometries, including a reference configuration, three layouts with varying aspect ratios and three layouts with different span ratios, accompanied with comparisons of acquired wind loads between the 2-way coupling FSI and the CFD-only simulation. Differences in the C_{Fx} values and the minimum C_p values induced by steady-state FSI effects are noticeable in cases with the higher L/B values and all cases of varying H/B values, indicating FSI effects on structural wind pressure distributions. Meanwhile, FSI effects on the C_{Fz} values and the maximum C_p values are fairly slight for these varying geometries.

Since structural wind loads and responses are usually maximum and symmetric along the x axis with the wind direction, properties only along the x axis are analyzed here. C_p values along the x axis with varying geometries are presented in Fig. 11. With variations in the aspect ratio, structural wind suction coefficients increase as the L/B rises from 1:1 to 2:1, while remain nearly unchanged when the aspect ratio further increases from 2:1 to 2.5:1. As for the FSI effect, differences between structural wind responses with and without FSI are insignificant with the lowest aspect ratio 1:1. In such case, magnitudes of structural stiffness to resist extra loads are the same along the two orthogonal directions, result in the synergistic effect on enhancing structural stiffness. Structural deformation gets lower in this way, and the FSI effect also become less pronounced. By contrast, the steady-state FSI effect become more pronounced as L/B rises, which can be attribute to increasing differences of structural stiffness along the two orthogonal directions. It can be presumed that structural wind pressure distributions may approximate results of the two-dimensional case when L/B increases to infinity. Depicted in Fig. 11(b), increases in structural wind

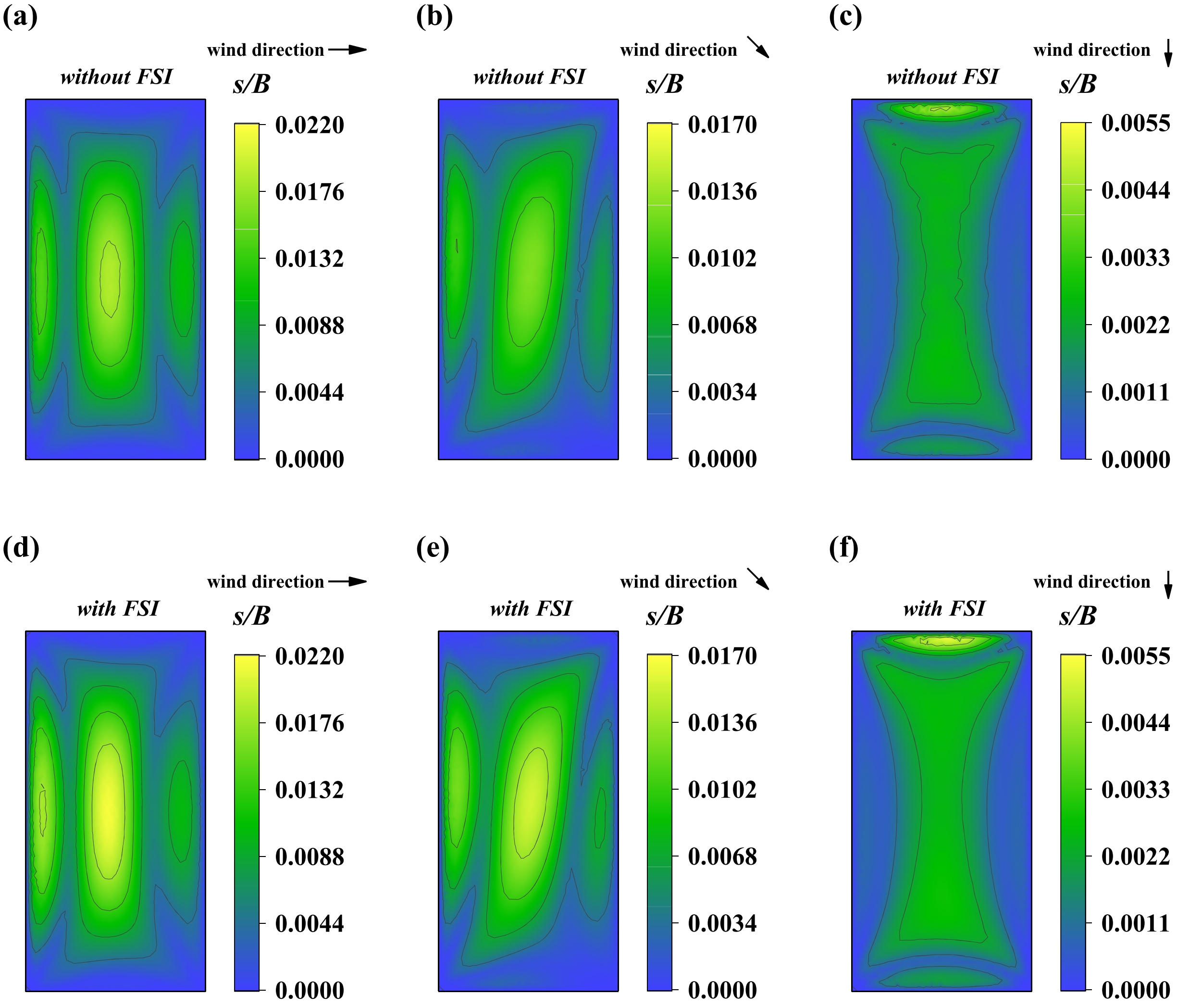

Fig. 9. Steady-state FSI effects on structural wind-induced displacements with different wind directions. (a) 0°, 1-way simulation; (b) 45°, 1-way simulation; (c) 90°, 1-way simulation; (d) 0°, 2-way coupling FSI; (e) 45°, 2-way coupling FSI; (f) 90°, 2-way coupling FSI.

pressures at windward and top locations are noticeable with rising span ratios, as structural geometries become blunter with higher H/B values, hence resulting in more intensive flow separations. Correspondingly, within all the four cases of varying H/B, variations in wind loads induced by steady-state FSI effects are also remarkable at these locations with noticeable wind pressures.

Table 9 gives structural response amplification factors β_s and β_ε with varying geometries, and Fig. 12 depicts wind-induced displacements and structural principal strain along the x axis of different geometries with and without FSI. The β_ε values obviously increase with cases of higher aspect ratios, which is similar with variation patterns of wind pressure coefficients. Nevertheless, variations of the β_ε values with L/B are rather complex due to different distribution patterns of structural wind responses. With aspect ratios of 1:1, 1.5:1 and 2:1, the maximum principal strain appears at the top center of the membrane, and higher FSI-induced amplification factors of structural strain are discovered. However, the maximum strain value is observed at the windward edge when the L/B is equal to 2.5:1, and the strain amplification effect disappears within such case. The β_s value decreases with higher span ratios, but structural maximum wind-induced displacements have still increased by more than 14 % within all cases of varying H/B. Variations of β_ε values are also related to the distribution patterns of structural principal strain, and higher amplification of structural strain is observed when ε_{max} appears at top locations. As in the following discussions, locations of maximum structural wind responses can play a crucial role in variation patterns of β_s and β_ε values.

4.3. Effects of wind pressures, internal pressures and membrane tensile stiffness

For ASMS, membrane is tensioned by the pressure difference to resist wind actions. Therefore, the combined effects of wind pressure, internal pressure and membrane elasticity are significant for structural wind-resistant performances. In following discussions, 210 cases with different wind velocities, internal pressures and membrane tensile stiffness are implemented to investigate the combined influence of the steady-state FSI effect. Table 10 presents the simulation parameters and corresponding similarity analysis. Values for the span B, the wind velocity U_r and the internal pressure P_{in} are realizable for the full-scale structures. The lower limit of membrane elastic modulus E_m for the prototype is less than values in practice (usually around 1000 MPa), and adopting this lower limit is intended to observe the more pronounced FSI effect. The upper limit of E_m values for the prototype is much higher than values of the membrane in the prototype scale. However, with the equal-stiffness principle, a higher E_m value can represent effects of cable reinforcements on ASMS.

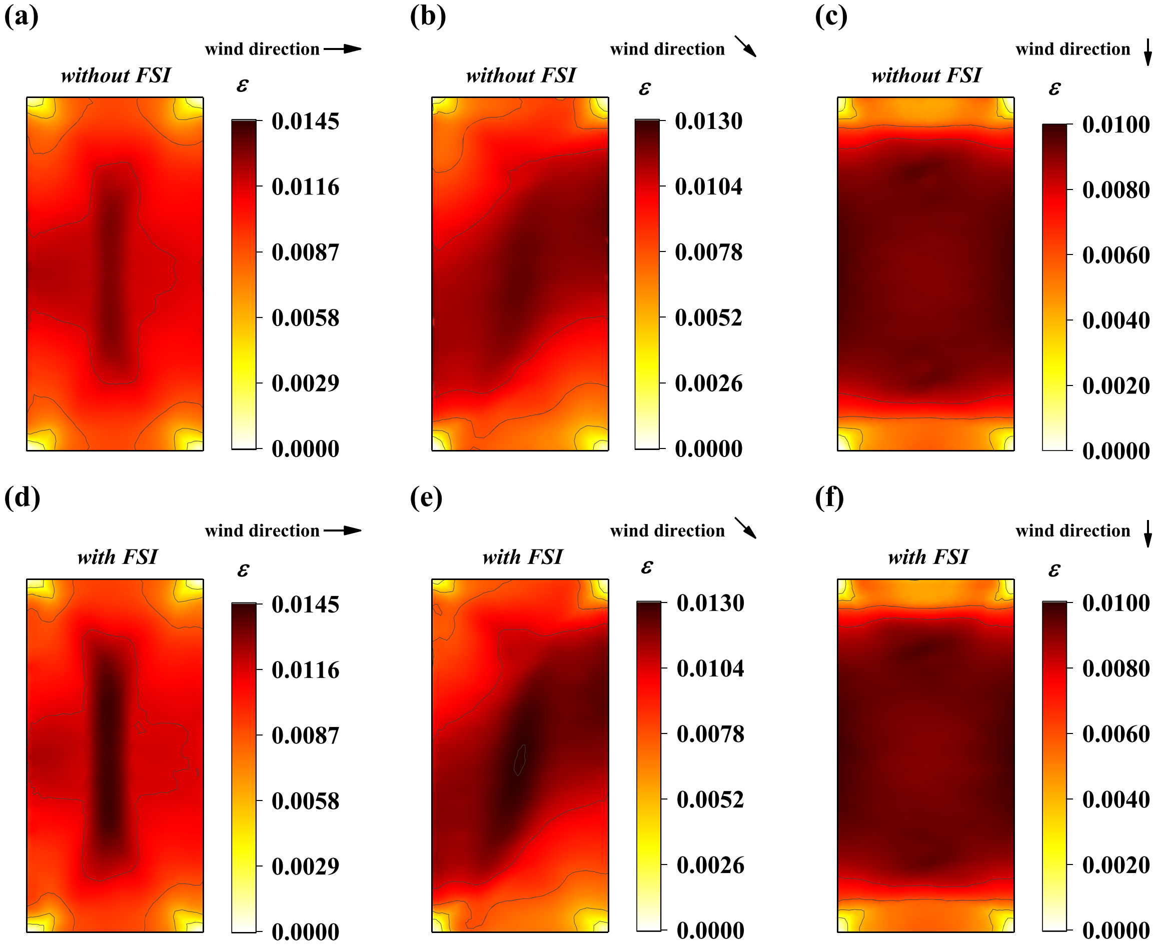

Fig. 10. Steady-state FSI effects on structural strain distribution with different wind directions. (a) 0°, CFD 1-way simulation; (b) 45°, CFD 1-way simulation; (c) 90°, CFD 1-way simulation; (d) 0°, 2-way coupling FSI; (e) 45°, 2-way coupling FSI; (f) 90°, 2-way coupling FSI.

Table 7
Steady-state FSI effects on wind responses with varying wind directions.

Wind direction	s_{max}/B $(\times 10^{-3})$		β_s	ε_{max} $(\times 10^{-3})$		β_ε
	FSI	without FSI		FSI	without FSI	
0°	21.6	18.6	1.16	14.3	13.2	1.08
15°	21.0	17.9	1.18	14.7	13.7	1.07
30°	19.7	16.2	1.21	14.4	13.3	1.07
45°	15.5	12.8	1.21	13.0	12.3	1.06
60°	9.9	8.5	1.16	11.5	11.4	1.01
75°	4.8	4.4	1.08	10.5	10.5	1.00
90°	5.2	4.8	1.08	9.8	9.7	1.01

4.3.1. *Influences on wind actions*

Fig. 13 presents wind load characteristics with different wind pressures, internal pressures and membrane tensile stiffness. Two dimensionless numbers, $P_{in}/\left(\rho U_r^2\right)$ and $E_m h/\left(\rho U_r^2 B\right)$, are applied to describe combined influences of the U_r, P_{in} and $E_m h$ parameters. Wind load characteristics vary smoothly with $P_{in}/\left(\rho U_r^2\right)$ and $E_m h/\left(\rho U_r^2 B\right)$, and hence indicating that high wind velocities, less internal pressures and increasing membrane flexibility can contribute to more intensive FSI effects. Larger magnitudes of horizontal wind force coefficients C_{Fx} and wind suction force coefficients are observed with lower $P_{in}/\left(\rho U_r^2\right)$ and $E_m h/\left(\rho U_r^2 B\right)$, while variations of C_{Fz} and maximum C_p values are relatively milder.

Fig. 14 presents some examples of wind pressure distribution and wind velocity in the xOz plane ($y = 0$) obtained by steady-state FSI

Table 8
Steady-state FSI effects on wind load characteristics with varying geometries.

Configurations	L (m)	B (m)	H (m)	C_{Fx}		C_{Fz}		Maximum C_p		Minimum C_p	
				FSI	CFD	FSI	CFD	FSI	CFD	FSI	CFD
Reference geometry	1.2	0.6	0.2	0.21	0.17	0.49	0.49	0.64	0.64	−1.59	−1.29
Varying aspect ratio L/B	0.6	0.6	0.2	0.13	0.13	0.40	0.40	0.71	0.71	−0.90	−0.87
	0.9			0.17	0.15	0.45	0.45	0.65	0.64	−1.34	−1.18
	1.5			0.25	0.20	0.51	0.52	0.64	0.63	−1.65	−1.33
Varying span ratio H/B	1.2	0.6	0.1	0.12	0.10	0.29	0.27	0.50	0.48	−0.99	−0.78
			0.15	0.16	0.13	0.39	0.39	0.58	0.57	−1.31	−1.08
			0.25	0.26	0.20	0.57	0.60	0.70	0.69	−1.78	−1.48

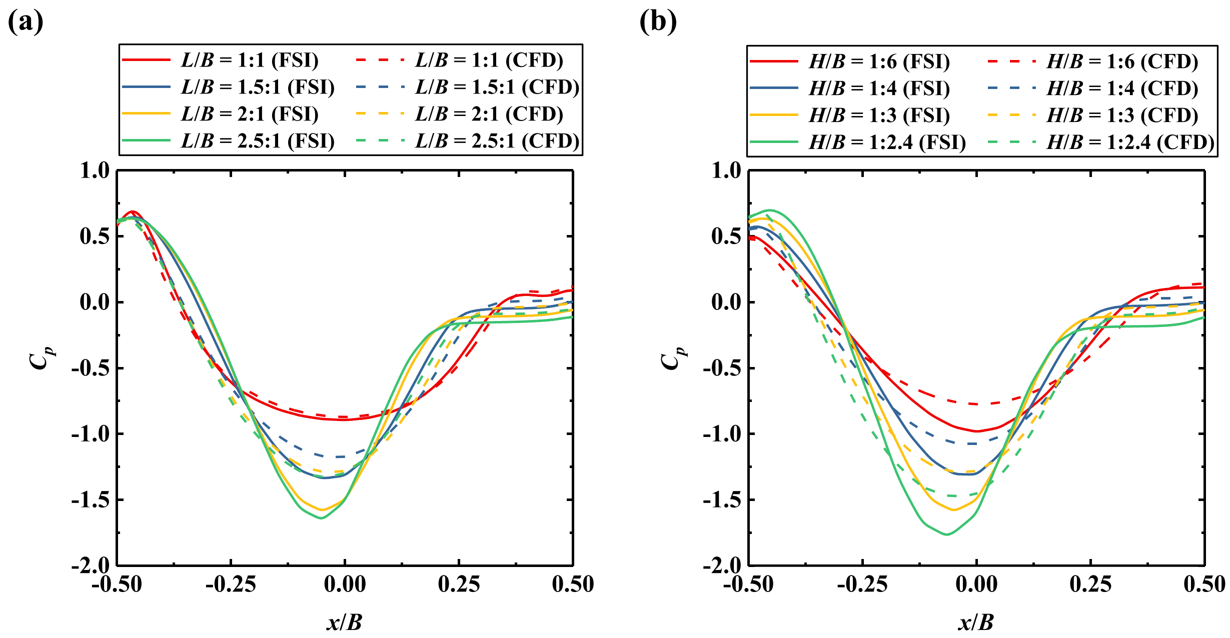

Fig. 11. Cp values along the x axis with varying geometries acquired by 2-way coupling FSI and CFD-only simulations. (a) Varying L/B; (b) Varying $H\ /B$.

Table 9
Steady-state FSI effects on wind responses with varying geometries.

Configurations	L (m)	B (m)	H (m)	s_{max}/B ($\times10^{-3}$)		β_s	ε_{max} ($\times10^{-3}$)		β_ε
				FSI	without FSI		FSI	without FSI	
Reference geometry	1.2	0.6	0.2	21.6	18.6	1.16	14.3	13.2	1.08
Varying aspect ratio L/B	0.6	0.6	0.2	7.1	6.7	1.05	10.6	10.3	1.02
	0.9			14.7	13.0	1.13	15.7	14.4	1.09
	1.5			23.9	20.7	1.16	14.4	14.4	1.00
Varying span ratio H/B	1.2	0.6	0.1	11.9	9.7	1.23	17.5	16.9	1.03
			0.15	16.2	13.8	1.18	14.6	14.4	1.02
			0.25	27.5	24.2	1.14	17.6	16.2	1.09

simulations. Results of the CFD-only simulation are also presented to serve reference, as depicted in Fig. 14(a). Fig. 14(b) is the case with both higher internal pressure and membrane tensile stiffness, in which slight FSI effects are observed compared with the rigid model. However, as the internal pressure decreases and the wind velocity gets higher as Fig. 14(c), noticeable deformations with buckling at the windward surface and lifting at the top locations appear on the structure, and wind suctions at top center are with higher magnitudes due to more intensive flow separations. In this way, these effects can result in increasing wind force coefficients C_{Fx} and lower values of the minimum C_p values. When further lowering the membrane tensile stiffness as in Fig. 14(d), more pronounced FSI effects are observed compared with Fig. 14(c) as a result of larger structural deformations.

4.3.2. *Influences on wind responses*

Compared with relatively monotonic changes in wind load distributions, steady-state FSI influences on structural wind responses are more complex due to noticeable geometric nonlinearity within ASMS. Fig. 15(a) and (b) present results of response amplification factors β_s and β_ε with varying $P_{in}/\left(\rho U_r^2\right)$ and $E_m h/\left(\rho U_r^2 B\right)$. Steady-state FSI effects can contribute to the increases of structural maximum wind-induced displacements and principal strain by up to 64 % and 17 %, respectively. It deserves attention that compared with wind load parameters, the β_s and β_ε values do not change with the two dimensionless numbers monotonically, which can be explained by varying locations of structural maximum responses.

Figs. 16 and 17 give two examples with different locations of structural maximum wind responses. For Fig. 16, the internal pressure is sufficient to maintain the original structural geometry when subjected to wind actions. Despite obvious displacements in the windward zone, the maximum wind-induced displacement occurs at the top center. Meanwhile, the principal strain distribution is relatively uniform for the example in Fig. 16, where the ε_{max} appears at the windward edge. With respect to the steady-state FSI effect, the structural maximum wind-induced displacement increases by 12 % when considering FSI, and the maximum principal strain remains nearly unchanged.

However, structures with lower internal pressures exhibit quite different wind response characteristics due to varying locations of structural maximum responses. Within the case displayed in Fig. 17, the internal pressure is obviously lower than the wind pressure. Hence, the structure experiences significant deformations at windward locations, contributing to noticeable FSI effects. Similar to the case depicted in Fig. 14(c), the 'caving' of windward surface and the lifting top zone can remarkably modify the wind pressure distribution, and the structural maximum wind-induced displacement has increased by 50 % when considering FSI. Moreover, the principal strain distribution also becomes uneven with lower internal pressures. ε_{max} appears at the top center location, and the steady-state FSI effect has contributed to the increase of structural strain by up to 15 % compared with results of the 1-way simulation.

As further illustrations, Fig. 18 displays the locations where structural maximum deformation or strain occurs within all cases of Fig. 15, which are expressed with the x-coordinate. Distinct straight-line boundaries are observed in Fig. 18, separating datapoints into

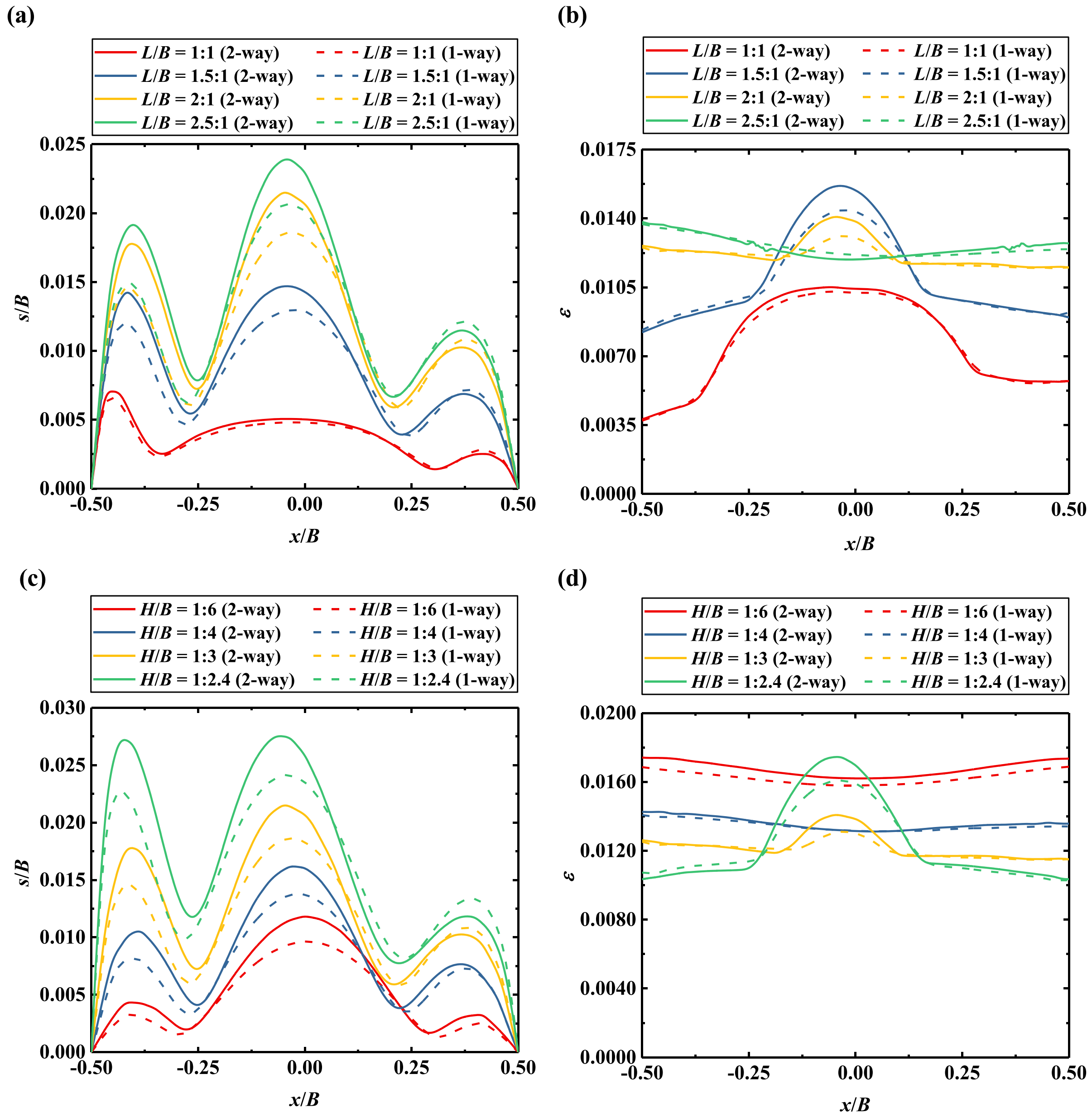

Fig. 12. Wind induced deformation and structural strain along the x axis with varying geometries acquired by 2-way coupling FSI and 1-way simulations. (a) Wind-induced deformation (varying L/B); (b) Structural strain (varying L/B); (c) Wind-induced deformation (varying H/B); (d) Structural strain (varying $H\ /B$).

Table 10
Parameters and similarity analysis on simulations with varying wind velocities, internal pressures and membrane tensile stiffness.

Property	Scaling ratio	Values (scaled model)	Values (prototype)
Geometry $L \times B \times H$	1:100	1.2 m × 0.6 m × 0.2m	120 m × 60 m × 20 m
Wind velocity U_r	1:2	6~18 m/s	12~36 m/s
Internal pressure P_{in}	1:4	50~300 Pa	200~1200 Pa
Membrane tensile stiffness $E_m h$	1:400	(0.1~6.4) × 10^4 N/m	(0.4~25.6) × 10^6 N/m
Membrane thickness h	1:100	10^{-5} m	10^{-3} m
Membrane elastic modulus E	1:4	100~6400 MPa	400~25,600 MPa

subgroups in which the maximum response occurs at windward or top locations. The boundary line can be obtained by regressions using sigmoid functions:

$$\widehat{f}\left(\frac{P_{in}}{\rho U_r^2},\frac{E_m h}{\rho U_r^2 B}\right)=\frac{1}{1+\exp\left[a_0+a_1\ln\left(\frac{P_{in}}{\rho U_r^2}\right)+a_2\ln\left(\frac{E_m h}{\rho U_r^2 B}\right)\right]} \tag{15}$$

The fitting function $\widehat{f}\left(\frac{P_{in}}{\rho U_r^2},\frac{E_m h}{\rho U_r^2 B}\right)$ is expected to approximate the indicator function $f\left(\frac{P_{in}}{\rho U_r^2},\frac{E_m h}{\rho U_r^2 B}\right)$. Referring to Fig. 18, f is empirically set as 0 where x_{max}/B is less than -0.25, and as 1 for other data points. The parameter set (a_0, a_1, a_2) can thus be obtained by fitting $\widehat{f}$ to f using the minimum least square approach, and the boundary line is obtained as $a_0+a_1\ln\left(\frac{P_{in}}{\rho U_r^2}\right)+a_2\ln\left(\frac{E_m h}{\rho U_r^2 B}\right)=0$, with expressions in both subfigures of Fig. 18. This boundary line can also provide insights into the complex

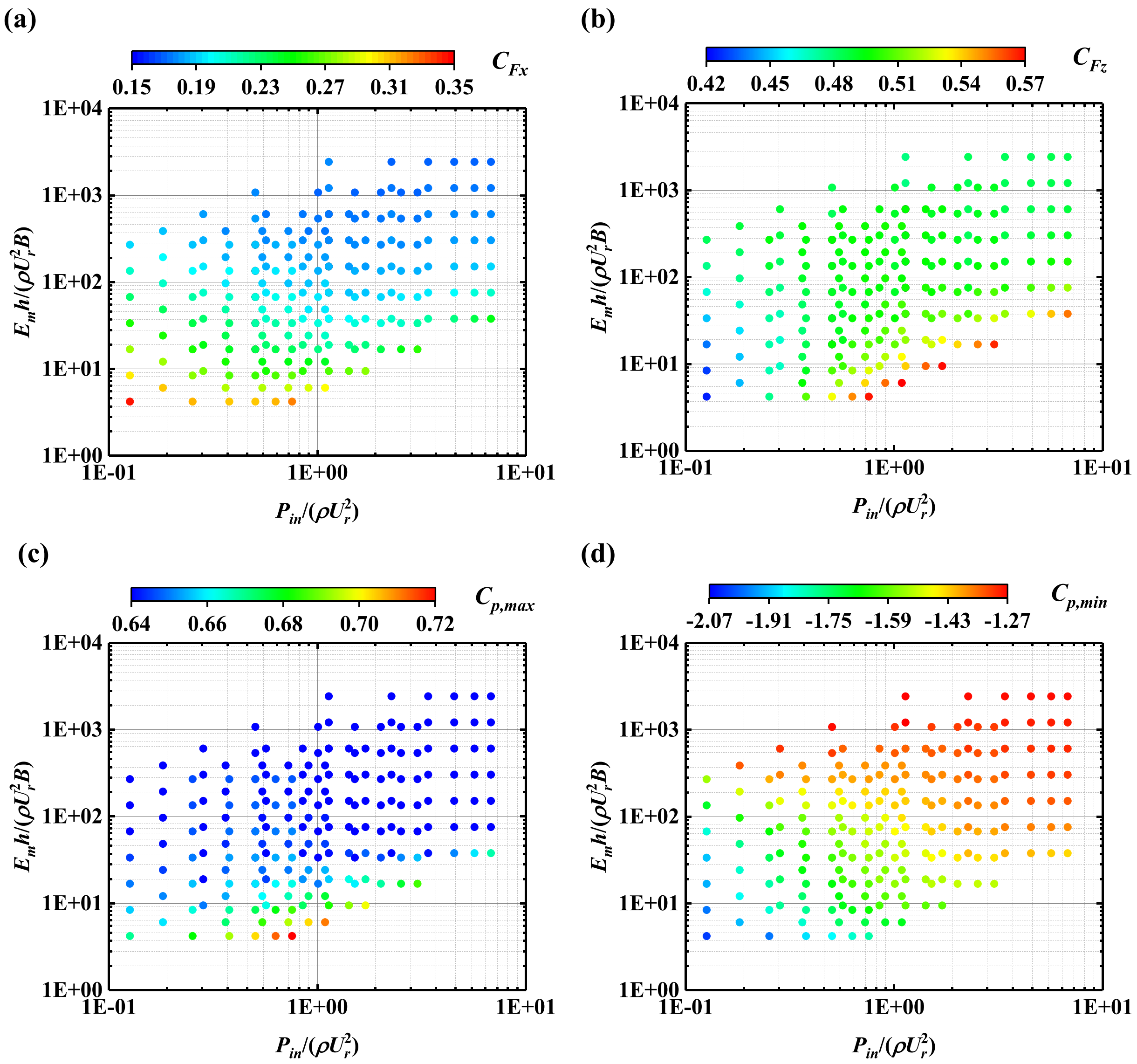

Fig. 13. Effects of $P_{in}/\left(\rho U_r^2\right)$ and $E_m h/\left(\rho U_r^2 B\right)$ on wind loads acquired by steady-state 2-way FSI simulations. (a) Wind force coefficient along *x*-axis C_{Fx}; (b) Wind force coefficient along *z*-axis C_{Fz}; (c) Max wind pressure coefficient $C_{p,max}$; (d) Min wind pressure coefficient $C_{p,min}$.

variation patterns of β_s and β_ε shown in Fig. 15. Compared with the uneven patterns of all the dataset, β_s and β_ε values vary relatively smoothly with the $P_{in}/\left(\rho U_r^2\right)$ and $E_m h/\left(\rho U_r^2 B\right)$ values at each side of these boundaries. Moreover, boundary within the two subfigures are different, and a noticeable finding is that the case of 0° wind direction presented in Figs. 9 and 10 (i.e., $P_{in}/\left(\rho U_r^2\right) = 0.57$, $E_m h/\left(\rho U_r^2 B\right) = 37.8$) is an intermediate scenario between results in Figs. 16 and 17, where the location belong to the maximum displacement is in Zone II, while the point corresponding to the max strain occurs in Zone I.

These discussions on variations in wind pressures, internal pressures and membrane tensile stiffness presented above involve two aspects of the steady-state FSI effects on ASMS: (1) structural deformations induced by the difference between the wind pressure and internal pressure, for example, the 'caving' at windward locations; (2) structural expansion when the membrane tensile stiffness value becomes extremely low. Though theoretically instructive, the latter part seems less significant in engineering practice, as the membrane of the full-scale structure is normally with high tensile stiffness. However, effects of the first part deserve attentions in the wind-resistant design. The disparate wind response patterns above are similar to the buckling of shell structures, as structural load-displacement relation varies significantly when extra load exceed certain values. The buckling has also been observed some studies on ASMS, as the windward surface caves in as wind pressures get higher than internal pressures [1,69]. Buckling usually leads to irreversible deformations and even structural failure when referring to shell structures. In contrast, it seems that the buckling in ASMS is unlikely to result in irreversible effects, as the air supply system and membrane geometric nonlinearity enable the real-time adjustment of structural stiffness in response to extra loads. Nevertheless, as depicted in Fig. 14, structural deformations lead to increased air separation and stronger wind actions when buckling occurs. Thus, steady-state FSI can still contribute to more pronounced amplifications of structural wind responses and uneven distributions of structural strain or stress. With the perspective of engineering application, even high-power air-supplying systems of ASMS can increase structural wind resistance by applying higher internal pressures, wind pressures can still eventually exceed the capacity of these facilities if an extremely harsh weather occurs. The buckling thus appears, and attentions should be paid to the amplification of time-averaged wind responses due to FSI. It should be remarked that the computational costs of carrying out steady-state FSI simulations are much less than the transient counterparts, enabling easy applications of these simulations in practice if one

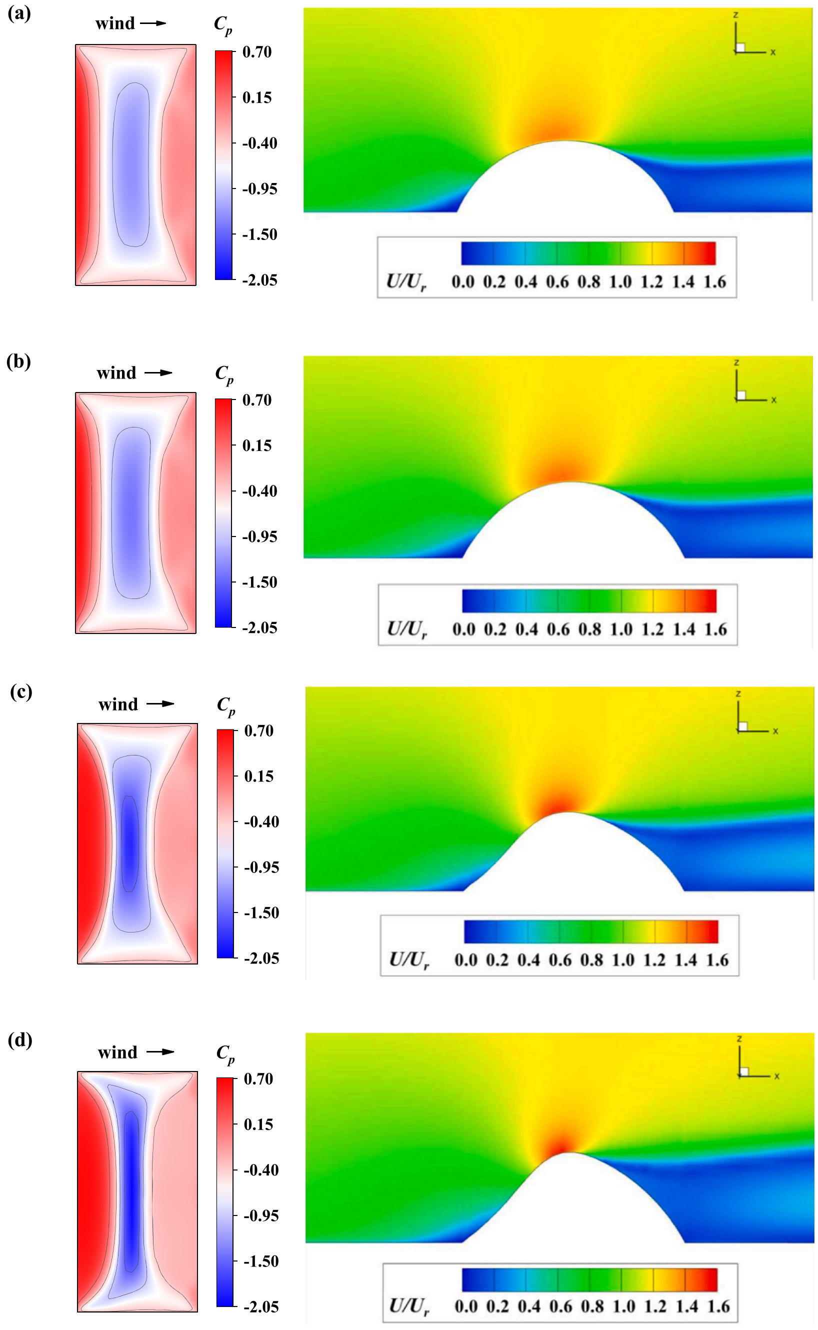

Fig. 14. Time-averaged C_p distributions and wind velocities in the *xOz* section obtained with CFD or steady-state 2-way FSI simulations. (a) The rigid model without FSI effects; (b) $P_{in}/\left(\rho U_r^2\right) = 1.42$, $E_m h/\left(\rho U_r^2 B\right) = 151.2$; (c) $P_{in}/\left(\rho U_r^2\right) = 0.13$, $E_m h/\left(\rho U_r^2 B\right) = 67.2$; (d) $P_{in}/\left(\rho U_r^2\right) = 0.13$, $E_m h/\left(\rho U_r^2 B\right) = 4.2$.

concerns the time-averaged response only.

Before concluding this study, some discussions are required on the applicability of the steady-state FSI simulation method. Based on previous aeroelastic wind tunnel studies [25,43,44], both aeroelastic instability and buffeting patterns of wind responses have been observed on ASMS. When aeroelastic instability appears, significant dynamic aeroelasticity effects might result in extra modifications on time-averaged wind actions, and the steady-state FSI simulation seems inapplicable because of its time-averaged approach. However, by referring material properties of ASMS in practice, air-supported membrane structures in engineering applications are usually with much higher stiffness. Hence, combining aeroelastic experiment results and similarity analysis, aeroelastic instability is unlikely to occur for ASMS at the prototype scale. In this way, ASMS exhibits the buffeting pattern, and the coupling between time-averaged and fluctuating components of wind actions becomes much less significant. Thus, the steady-state FSI simulation is still reliable for ASMS structures in practice.

5. Concluding remarks

With the perspective of static aeroelasticity and motivated to investigate the time-averaged part of wind-induced FSI effects on the air-supported membrane structure (ASMS), this work carries out steady-state FSI simulations to obtain wind loads and responses with the case of rectangular-planed configuration. Coupling the steady-state CFD and FEM modules, the computational inexpensive steady-state FSI simulations have been performed and successfully validated with aeroelastic wind tunnel experiments. Results have underscored the necessity of

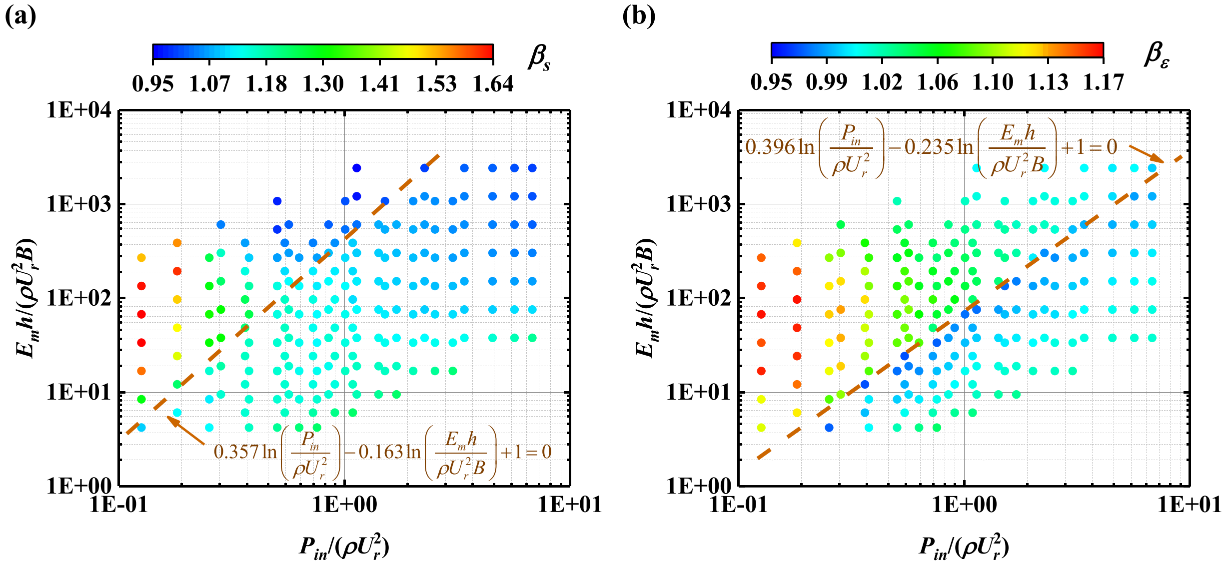

Fig. 15. Influences of $P_{in}/(\rho U_r^2)$ and $E_m h/(\rho U_r^2 B)$ on FSI-induced wind response amplification factors. (a) Displacement amplification factor β_s; (b) Strain amplification factor β_ε.

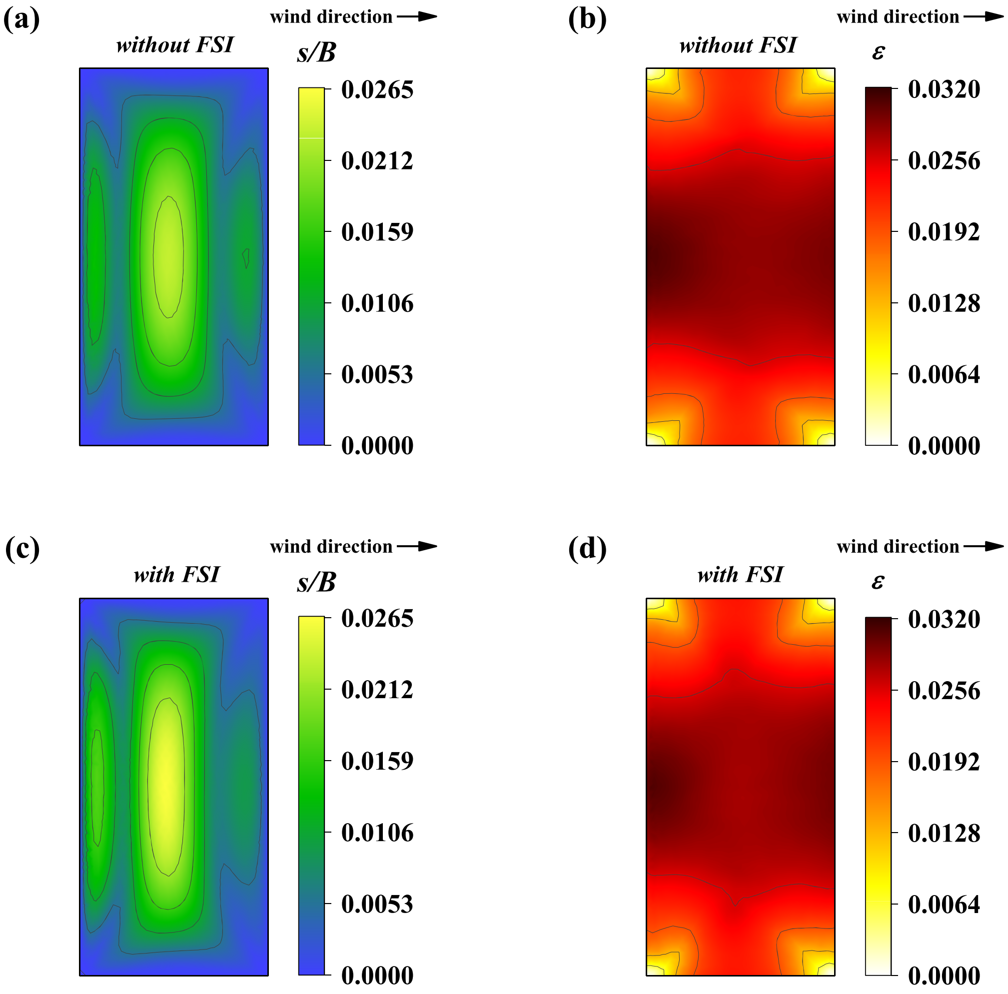

Fig. 16. Structural wind response distributions with $P_{in}/(\rho U_r^2) = 0.63$, $E_m h/(\rho U_r^2 B) = 16.8$ ($\beta_s = 1.12$, $\beta_\varepsilon = 0.98$). (a) Wind-induced displacements (without FSI); (b) Principal strain (without FSI); (c) Wind-induced displacements (with FSI); (d) Principal strain (with FSI).

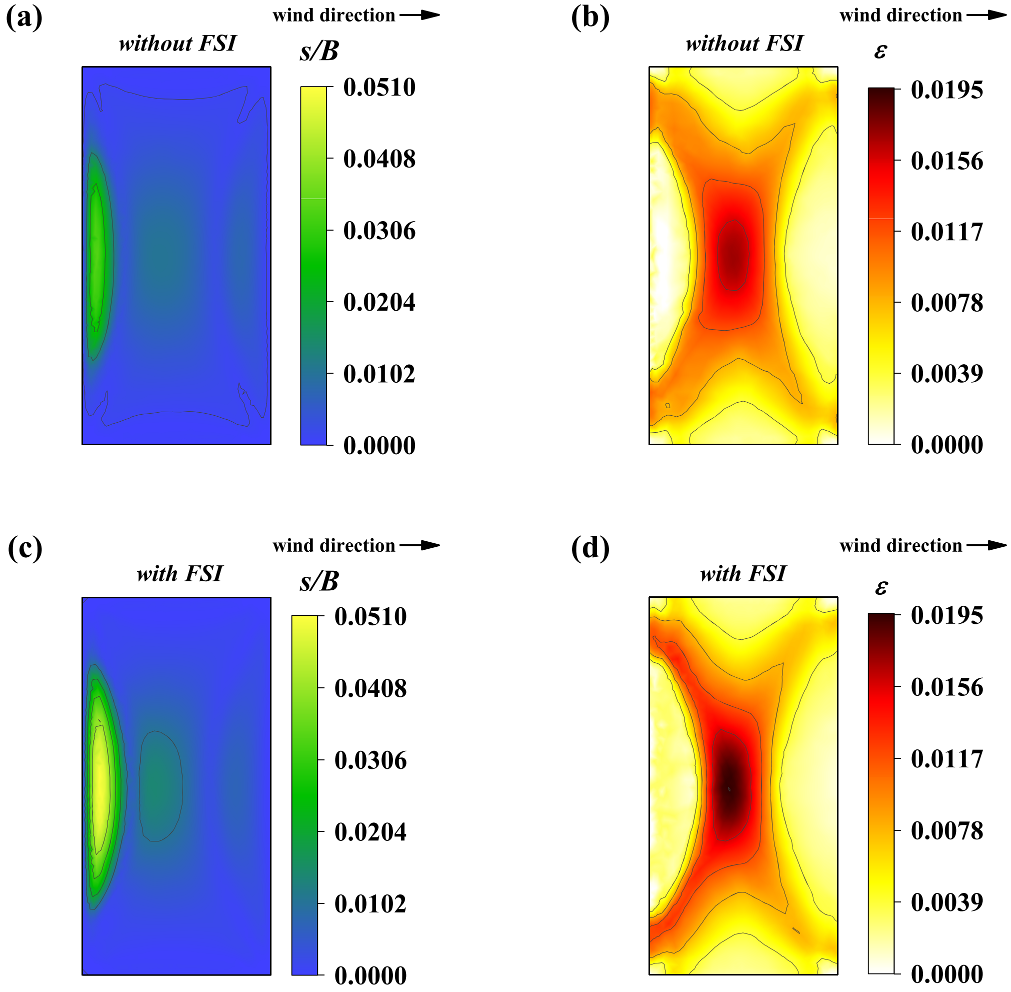

Fig. 17. Structural wind response distributions with $P_{in}/(\rho U_r^2) = 0.13$, $E_m h/(\rho U_r^2 B) = 67.2$ ($\beta_s = 1.50$, $\beta_\varepsilon = 1.15$). (a) Wind-induced displacements (without FSI); (b) Principal strain (without FSI); (c) Wind-induced displacements (with FSI); (d) Principal strain (with FSI).

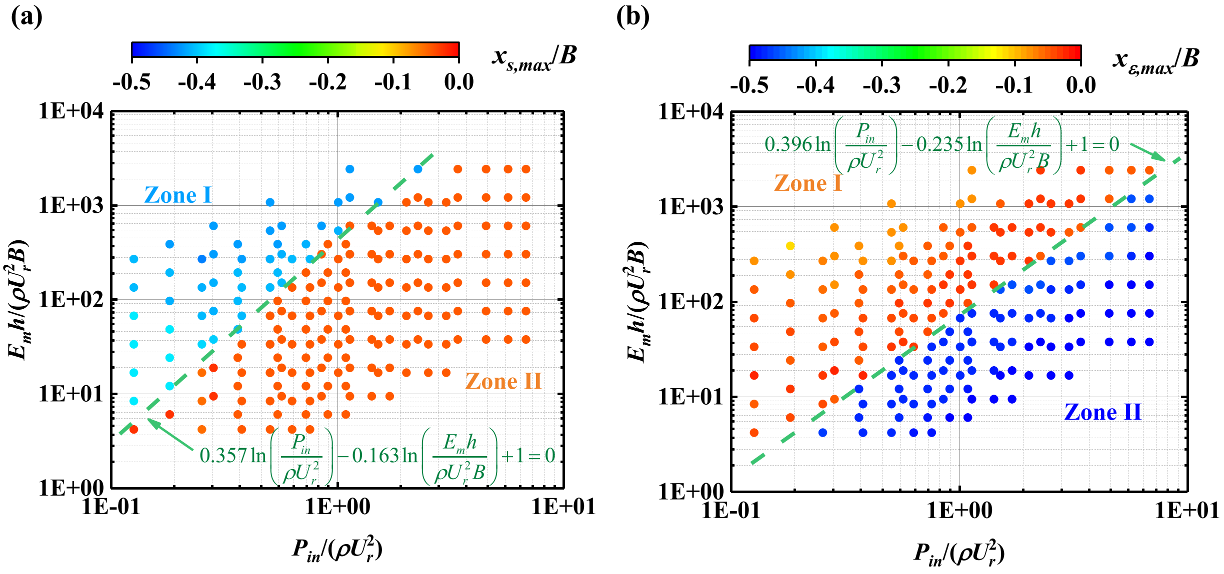

Fig. 18. Effects of $P_{in}/(\rho U_r^2)$ and $E_m h/(\rho U_r^2 B)$ on locations of structural max wind responses. (a) x coordinate of the s_{max} location; (b) x coordinate of the ε_{max} location.

accounting the steady-state FSI influences on wind action, as amplifications of structural wind pressure, wind-induced displacement and principal strain are observed when comparing with 1-way simulation results.

After validating the feasibility and necessity of performing steady-state FSI simulations, factors influencing steady-state FSI effects are investigated. Amplification effects of FSI on steady-state wind loads and structural responses are more noticeable when structural stiffness to resist wind actions gets lower, as discovered on cases with the 0° wind direction, lower aspect ratios, larger span ratios, less internal pressures and reduced membrane tensile stiffness. Moreover, as ASMS is characterized by combined influences of wind pressures, internal pressures and membrane tensile stiffness, effects of two nondimensional numbers, $P_{in}/(\rho U_r^2)$ and $E_m h/(\rho U_r^2 B)$, are investigated. Wind load characteristics vary smoothly with these two numbers, while variations of FSI-induced wind response amplification factors are rather complex. Steady-state FSI-induced amplification effects on structural wind responses are more pronounced when the buckling at windward surface occurs, usually observed on cases with insufficient internal pressures.

The contribution of this study is to highlight the importance of steady-state FSI for ASMS subjected to wind actions. On the one hand, amplifications on structural time-averaged wind responses induced by static aeroelasticity should be considered in practice, especially during harsh conditions where wind pressures are comparable or even larger than internal pressures. On the other hand, these amplification effects can be easily solved using steady-state FSI simulations with realizable computational efforts, while preserving reliable accuracy with respect to time-averaged component of wind actions.

CRediT authorship contribution statement

Keye Yan: Writing – original draft, Visualization, Validation, Software, Methodology, Investigation, Formal analysis, Data curation. **Yue Wu:** Writing – review & editing, Supervision, Resources, Project administration, Funding acquisition, Conceptualization. **Qiming Zhu:** Writing – review & editing, Supervision, Project administration, Conceptualization. **Zhaoqing Chen:** Resources, Funding acquisition, Data curation. **Boo Cheong Khoo:** Writing – review & editing, Conceptualization.

Declaration of competing interest

The authors declare that they have no known competing financial interests or personal relationships that could have appeared to influence the work reported in this paper.

Data availability

Data will be made available on request.

Acknowledgments

This research is supported by the National Natural Science Foundation of China (Grant No. 51878129, 52178163, 52378144), Chinese Scholarship Council (Grant No. 202306120243), Foundation of Key Laboratory of Structures Dynamic Behavior and Control (Ministry of Education) in Harbin Institute of Technology (Grant No. HITCE202004)

References

[1] M.J. Cook, The Design of Air Supported Structures to Resist Wind Loading, University of Bath, 1983. Ph.D. thesis.

[2] Y. Yin, W. Chen, J. Hu, B. Zhao, Q. Wang, In-situ measurement of structural performance of large-span air-supported dome under wind loads, Thin-Walled Struct 169 (2021) 108476, https://doi.org/10.1016/j.tws.2021.108476.

[3] X. Li, Y. Wang, Q. Chu, S. Xue, Y. He, Wind-induced response monitoring of large-span air-supported membrane structure coal-shed under the influence of typhoons, Thin-Walled Struct 181 (2022) 190051, https://doi.org/10.1016/j.tws.2022.109951.

[4] R. Bisplinghoff, H. Ashley, R. Halfman, Aeroelasticity, Addison-Wesley, Reading, MA, 2015.

[5] A.R. Collar, The expanding domain of aeroelasticity, Aeronaut. J. 50 (428) (1946) 613–636, https://doi.org/10.1017/S0368393100120358.

[6] D. Li, Z. Lai, C. Liu, J. Guo, X. Yang, M. Guan, Random vibration of pretensioned rectangular membrane structures under heavy rainfall excitation, Thin-Walled Struct. 164 (2021) 107856, https://doi.org/10.1016/j.tws.2021.107856.

[7] D. Li, Z. Zheng, M. Todd, Nonlinear vibration of orthotropic rectangular membrane structures including modal coupling, J. of Appl. Mechanics-Transactions of the ASME 85 (2018) 061004, https://doi.org/10.1115/1.4039620.

[8] R.H. Scanlan, J.J. Tomko, Airfoil and Bridge Deck Flutter Derivatives, J. Eng. Mech. Div. 97 (6) (1971) 1717–1737, https://doi.org/10.1061/JMCEA3.0001526.

[9] E. Guilmineau, P. Queutey, A numerical simulation of vortex shedding from an oscillating circular cylinder, J. Fluids Struct. 16 (6) (2002) 773–794, https://doi.org/10.1006/jfls.2002.0449.

[10] S. Dong, G.E. Karniadakis, DNS of flow past a stationary and oscillating cylinder at $Re = 10\ 000$, J. Fluids Struct. 20 (2005) 519–531, https://doi.org/10.1016/j.jfluidstructs.2005.02.004.

[11] S. Kumar, N. Navrose, S. Mittal, Lock-in in forced vibration of a circular cylinder, Phys. Fluids 28 (2016) 113605, https://doi.org/10.1063/1.4967729.

[12] P.W. Bearman, S.C. Luo, Investigation of the aerodynamic instability of a square-section cylinder by forced oscillation, J. Fluids Struct. 2 (2) (1988) 161–176, https://doi.org/10.1016/S0889-9746(88)80017-3.

[13] Z. Chen, Y. Wang, S. Wang, H. Huang, K. Yuan, S. Li, C.Y. Li, Y. Xu, Fluid–structure interaction on vibrating square prisms considering interference effects, Phys. Fluids 35 (12) (2023) 125111, https://doi.org/10.1063/5.0179996.

[14] Z. Chen, J. Bai, Y. Xu, S. Li, J. Hua, C.Y. Li, X. Xue, Unsteady aerodynamic force on a transverse inclined slender prism using forced vibration, Wind Struct 37 (5) (2023) 331–346, https://doi.org/10.12989/was.2023.37.5.331.

[15] A. Jain, N.P. Jones, R.H. Scanlan, Coupled Flutter and Buffeting Analysis of Long-Span Bridges, J. Struct. Eng. 122 (7) (1996) 716–725, https://doi.org/10.1061/(ASCE)0733-9445(1996)122:7(716).

[16] G. Diana, S. Stoyanoff, K. Aas-Jakobsen, A. Allsop, M. Andersen, T. Argentini, M. C. Montoya, S. Hernández, J.A. Jurado, H. Katsuchi, I. Kavrakov, H. Kim, G. Larose, A. Larsen, G. Morgenthal, O. Øiseth, S. Omarini, D. Rocchi, M. Svendsen, T. Wu, IABSE Task Group 3.1 Benchmark Results. Part 1: numerical Analysis of a Two-Degree-of-Freedom Bridge Deck Section Based on Analytical Aerodynamics, Struct. Eng. Int. 30 (3) (2020) 401–410, https://doi.org/10.1080/10168664.2019.1639480.

[17] X. Chen, Estimation of stochastic crosswind response of wind-excited tall buildings with nonlinear aerodynamic damping, Eng. Struct. 56 (2013) 766–778, https://doi.org/10.1016/j.engstruct.2013.05.044.

[18] Q. Yang, K. Guo, W. Shan, Y.C. Kim, Y. Tamura, Identification of nonlinear aerodynamic damping of cross-wind excited slender structures in atmospheric boundary layer flow, J. Wind Eng. Ind. Aerodyn. 241 (2023) 105519, https://doi.org/10.1016/j.jweia.2023.105519.

[19] Z. Chen, S. Li, L. Zhang, C. Yuan, Z. Zhao, Y. Wu, Y. Xu, C.Y. Li, Characteristics of aerodynamic interference and flow phenomenology around inclined square prisms, Phys. Fluids 35 (12) (2023) 125119, https://doi.org/10.1063/5.0182197.

[20] J. Macdonald, G. Larose, A unified approach to aerodynamic damping and drag/lift instabilities, and its application to dry inclined cable galloping, J. Fluids Struct. 22 (2) (2006) 229–252, https://doi.org/10.1016/j.jfluidstructs.2005.10.002.

[21] F. Duan, Y. Song, S. Gao, Y. Liu, W. Chu, X. Lu, Z. Liu, Study on aerodynamic instability and galloping response of rail overhead contact line based on wind tunnel tests, IEEE Trans. Veh. Technol. 72 (6) (2023) 7211–7220, https://doi.org/10.1109/TVT.2023.3243024.

[22] H. Kuneida, Flutter of hanging roofs and curved membrane roofs, Int J Solids Struct 11 (4) (1975) 477–492, https://doi.org/10.1016/0020-7683(75)90083-9.

[23] H. Irwin, R.L. Wardlaw, A wind tunnel investigation of a retractable fabric roof for the Montreal Olympic stadium, in: Proceedings of the Fifth International Conference on Wind Engineering 2, 1980, pp. 925–938, https://doi.org/10.1016/B978-1-4832-8367-8.50087-5.

[24] Y. Uematsu, K. Uchiyama, Aeroelastic behavior of an h.p.-shaped suspended roof. shells, membranes and space frames, in: Proceedings IASS Symposium, Osaka 2, 1986, pp. 241–248.

[25] R. Sygulski, Dynamic stability of pneumatic structures in wind: theory and experiment, J. Fluids Struct. 10 (8) (1996) 945–963, https://doi.org/10.1006/jfls.1996.0060.

[26] H. Minami, Added mass of a membrane vibrating at finite amplitude, J. Fluids Struct. 12 (7) (1998) 919–932, https://doi.org/10.1006/jfls.1998.0175.

[27] Q. Yang, R. Liu, On aerodynamic stability of membrane structures, Int. J. Space Struct. 20 (3) (2005) 181–188, https://doi.org/10.1260/026635105775213782.

[28] Q. Yang, Y. Wu, W. Zhu, Experimental study on interaction between membrane structures and wind environment, Earthq. Eng. Eng. Vib. 9 (4) (2010) 523–532, https://doi.org/10.1007/s11803-010-0034-0.

[29] Y. Li, L. Wang, Z. Shen, Y. Tamura, Added-mass estimation of flat membranes vibrating in still air, J. Wind Eng. Ind. Aerodyn. 99 (8) (2011) 815–824, https://doi.org/10.1016/j.jweia.2011.05.006.

[30] Y. Zhou, Y. Li, Z. Shen, L. Wang, Y. Tamura, Numerical analysis of added mass for open flat membrane vibrating in still air using the boundary element method, J. Wind Eng. Ind. Aerodyn. 131 (2014) 100–111, https://doi.org/10.1016/j.jweia.2014.05.007.

[31] Y. Wu, Z. Chen, X. Sun, Research on the wind-induced aero-elastic response of closed-type saddle-shaped tensioned membrane models, J. Zhejiang Univ.-Sci. A 16 (2015) 656–668, https://doi.org/10.1631/jzus.A1400340.

[32] C. Liu, X. Deng, Z. Zheng, Nonlinear wind-induced aerodynamic stability of orthotropic saddle membrane structures, J. Wind Eng. Ind. Aerodyn. 164 (2017) 119–127, https://doi.org/10.1016/j.jweia.2017.02.422006.

[33] T. Li, Q. Yang, T. Ishihara, Unsteady aerodynamic characteristics of long-span roofs under forced excitation, J. Wind Eng. Ind. Aerodyn. 181 (2018) 46–60, https://doi.org/10.1016/j.jweia.2018.08.005.

[34] Y. Takadate, Y. Uematsu, Steady and unsteady aerodynamic forces on a long-span membrane structure, J. Wind Eng. Ind. Aerodyn. 193 (2019) 103946, https://doi.org/10.1016/j.jweia.2019.06.018.

[35] F. Rizzo, G.A. Kopp, G.F. Giaccu, Investigation of wind-induced dynamics of a cable net roof with aeroelastic wind tunnel tests, Eng. Struct. 229 (2021) 111569, https://doi.org/10.1016/j.engstruct.2020.111569.

[36] Q. Yang, T. Wang, B. Yan, T. Li, M. Liu, Nonlinear motion-induced aerodynamic forces on large hyperbolic paraboloid roofs using LES, J. Wind Eng. Ind. Aerodyn. 216 (2021) 104703, https://doi.org/10.1016/j.jweia.2021.104703.

[37] Z. Chen, Y. Su, J. Wang, N. Su, L. Tang, Experimental study on aeroelastic instability of spherical inflatable membrane structures with a large rise–span ratio, Buildings 12 (2022) 1336, https://doi.org/10.3390/buildings12091336.

[38] D. Li, Z. Zhang, C. Zhang, Z. Zhang, X. Yang, Aeroelastic experimental investigation of hyperbolic paraboloid membrane structures in normal and typhoon winds, Sustainability. 14 (2022) 12207, https://doi.org/10.3390/su141912207.

[39] K. Yan, Y. Wu, Z. Chen, J. Zhao, Analysis on aeroelastic stability of rectangular-planed air-supported membrane structures, Thin-Walled Struct. 195 (2024) 111416, https://doi.org/10.1016/j.tws.2023.111416.

[40] K. Hincz, M. Gamboa-Marrufo, Deformed shape wind analysis of tensile membrane structures, J. Struct. Eng. 142 (3) (2016) 04015153, https://doi.org/10.1061/(ASCE)ST.1943-541X.0001437.

[41] F. Sun, M. Gu, A numerical solution to fluid-structure interaction of membrane structures under wind action, Wind Struct 19 (1) (2014) 33–58, https://doi.org/10.12989/was.2014.19.1.035.

[42] G. De Nayer, A. Apostolatos, J.N. Wood, K.-U. Bletzinger, R. Wüchner, M. Breuer, Numerical studies on the instantaneous fluid–structure interaction of an air-inflated flexible membrane in turbulent flow, J. Fluids Struct. 82 (2018) 577–609, https://doi.org/10.1016/j.jfluidstructs.2018.08.005.

[43] M. Kassem, M. Novak, Response of hemispherical, air-supported structures to wind, J. Eng. Mech. 117 (8) (1991) 1718–1737, https://doi.org/10.1061/(ASCE)0733-9399(1991)117:8(1718).

[44] Y. Wu, K. Yan, Z. Chen, Aeroelastic wind tunnel investigations on rectangular-planed air-supported membrane structures, Thin-Walled Struct 190 (2023) 110955, https://doi.org/10.1016/j.tws.2023.110955.

[45] M. Glück, M. Breuer, F. Durst, A. Halfmann, E. Rank, Computation of fluid-structure on lightweight structures, J. Wind Eng. Ind. Aerodyn. 89 (2001) 1351–1368, https://doi.org/10.1016/S0167-6105(01)00150-7.

[46] M. Glück, M. Breuer, F. Durst, A. Halfmann, E. Rank, Computation of wind-induced vibrations of flexible shells and membranous structures, J. Fluids Struct. 17 (2003) 739–765, https://doi.org/10.1016/S0889-9746(03)00006-9.

[47] R. Wüchner, A. Kupzok, K.-U. Bletzinger, A framework for stabilized partitioned analysis of thin membrane–wind interaction, Int. J. Numer. Methods Fluids 54 (6–8) (2007) 945–963, https://doi.org/10.1002/fld.1474.

[48] A. Michalski, P.D. Kermel, E. Haug, R. Löhner, R. Wüchner, K.-U. Bletzinger, Validation of the computational fluid–structure interaction simulation at real-scale tests of a flexible 29m umbrella in natural wind flow, J. Wind Eng. Ind. Aerodyn. 99 (4) (2011) 400–413, https://doi.org/10.1016/j.jweia.2010.12.010.

[49] Q. Zhu, X. Wang, C. Demartino, J. Yan, Revealing aeroelastic effects on low-rise roof structures in turbulent winds via isogeometric fluid–structure interaction, Comput. Mech. 72 (2023) 1175–1190, https://doi.org/10.1007/s00466-023-02341-8.

[50] Q. Yang, F. Chen, Y. Tamura, T. Li, B. Yan, Fluid-structure interaction behaviors of tension membrane roofs by fully-coupled numerical simulation, J. Wind Eng. Ind. Aerodyn. 244 (2024) 105609, https://doi.org/10.1016/j.jweia.2023.105609.

[51] J.N. Wood, M. Breuer, G. De Nayer, Experimental studies on the instantaneous fluid–structure interaction of an air-inflated flexible membrane in turbulent flow, J. Fluids Struct. 80 (2018) 405–440, https://doi.org/10.1016/j.jfluidstructs.2018.02.006.

[52] G. De Nayer, M. Breuer, Assessment of discrete wind gust parameters: towards the worst-case scenario of a FSI application in form of an inflated hemisphere, J. Wind Eng. Ind. Aerodyn. 231 (2022) 105207, https://doi.org/10.1016/j.jweia.2022.105207.

[53] G. De Nayer, M. Breuer, K. Boulbrachene, FSI simulations of wind gusts impacting an air-inflated flexible membrane at $Re = 100{,}000$, J. Fluids Struct. 109 (2022) 103462, https://doi.org/10.1016/j.jfluidstructs.2021.103462.

[54] E. Lund, H. Møller, L. Jakobsen, Shape design optimization of stationary fluid-structure interaction problems with large displacements and turbulence, Struct. Multidiscipl. Optim. 25 (2003) 383–392, https://doi.org/10.1007/s00158-003-0288-5.

[55] G.H. Yoon, Topology optimization for stationary fluid–structure interaction problems using a new monolithic formulation, Int. J. Numer. Methods Eng. 82 (2010) 591–616, https://doi.org/10.1002/nme.2777.

[56] P.J. Maljaars, M.L. Kaminski, J.H. Den Besten, A new approach for computing the steady state fluid–structure interaction response of periodic problems, J. Fluids Struct. 84 (2019) 140–152, https://doi.org/10.1016/j.jfluidstructs.2018.10.002.

[57] I. López, J. Piquee, P. Bucher, K.-U. Bletzinger, C. Breitsamter, R. Wüchner, Numerical analysis of an elasto-flexible membrane blade using steady-state fluid–structure interaction simulations, J. Fluids Struct. 106 (2021) 103355, https://doi.org/10.1016/j.jfluidstructs.2021.103355.

[58] K.E.S. Silva, R. Sivapuram, S. Ranjbarzadeh, R.S. Gioria, E.C.N. Silva, R. Picelli, Topology optimization of stationary fluid–structure interaction problems including large displacements via the TOBS-GT method, Struct. Multidiscipl. Optim. 65 (2022) 337, https://doi.org/10.1007/s00158-022-03442-3.

[59] B. San, Q. Yang, L. Yin, Stochastic and sensitivity analysis of shape error of inflatable antenna reflectors, Acta Astronaut. 132 (2017) 170–176, https://doi.org/10.1016/j.actaastro.2016.12.015.

[60] Y. Yang, S. Qian, J. Gong, A new patterning technique of membrane structures for minimizing deviations of stress and shape, Thin-Walled Struct 151 (2020) 106741, https://doi.org/10.1016/j.tws.2020.106741.

[61] V. Yakhot, S.A. Orszag, S. Thangam, T.B. Gatski, C.G. Speziale, Development of turbulence models for shear flows by a double expansion technique, Phys. Fluids A: Fluid Dyn. 4 (1992) 1510–1520, https://doi.org/10.1063/1.858424.

[62] GB50009-2012, Load Code for the Design of Building Structures, China Architecture and Building Press, Beijing, China, 2012.

[63] ANSYS FLUENT 2020 R2 User's Guide, ANSYS Inc, 2020.

[64] B.V. Tryggvason, Aeroelastic modelling of pneumatic and tensioned fabric structures, in: Proceedings of the Fifth International Conference on Wind Engineering 2, 1980, pp. 1061–1072, https://doi.org/10.1016/B978-1-4832-8367-8.50098-X.

[65] Z. Chen, J. Zhao, K. Yan, Y. Wu, D. Zhang, N. Su, Wind tunnel test study on aero-elastic model of spherical inflatable membrane structures, J. Build. Struct. 44 (3) (2023) 137–147, https://doi.org/10.14006/j.jzjgxb.2021.0791. In Chinese.

[66] Z. Chen, P. Song, K. Yan, Y. Wu, N. Su, C. Zeng, Wind-induced aero-elastic response and vibration coefficients of capsule inflatable membrane structure, J. Vib. Eng. 37 (1) (2024) 31–39, https://doi.org/10.16385/j.cnki.issn.1004-4523.2024.01.004. In Chinese.

[67] CECS158:2015, Technical Specification for Membrane Structures, China Planning Press, Beijing, China, 2015.

[68] P.F. Luo, Y.J. Chao, M.A. Sutton, W.H. Peters, Accurate measurement of three-dimensional deformations in deformable and rigid bodies using computer vision, Exp. Mech. 33 (1993) 123–132, https://doi.org/10.1007/BF02322488.

[69] B.G. Newman, U. Ganguli, S.C. Shrivastava, Flow over spherical inflated buildings, J. Wind Eng. Ind. Aerodyn. 17 (3) (1984) 305–327, https://doi.org/10.1016/0167-6105(84)90023-0.